Biophysical Journal Volume 108 June 2015 2854–2864

Article

A Temperature-Jump Optical Trap for Single-Molecule Manipulation

Sara de Lorenzo,[1,2] Marco Ribezzi-Crivellari,[1] J. Ricardo Arias-Gonzalez,[3,4] Steven B. Smith,[5] and Felix Ritort[1,2,*]

[1]Departament de Física Fonamental, Universitat de Barcelona, Barcelona, Spain; [2]Ciber-BBN de Bioingenería, Biomateriales y Nanomedicina, Instituto de Salud Carlos III, Madrid, Spain; [3]Instituto Madrileño de Estudios Avanzados en Nanociencia (IMDEA Nanociencia), Cantoblanco, Madrid, Spain; [4]CNB-CSIC-IMDEA Nanociencia Associated Unit "Unidad de Nanobiotecnología", Madrid, Spain; and [5]Steven B. Smith Engineering, Los Lunas, New Mexico

ABSTRACT To our knowledge, we have developed a novel temperature-jump optical tweezers setup that changes the temperature locally and rapidly. It uses a heating laser with a wavelength that is highly absorbed by water so it can cover a broad range of temperatures. This instrument can record several force-distance curves for one individual molecule at various temperatures with good thermal and mechanical stability. Our design has features to reduce convection and baseline shifts, which have troubled previous heating-laser instruments. As proof of accuracy, we used the instrument to carry out DNA unzipping experiments in which we derived the average basepair free energy, entropy, and enthalpy of formation of the DNA duplex in a range of temperatures between 5°C and 50°C. We also used the instrument to characterize the temperature-dependent elasticity of single-stranded DNA (ssDNA), where we find a significant condensation plateau at low force and low temperature. Oddly, the persistence length of ssDNA measured at high force seems to increase with temperature, contrary to simple entropic models.

INTRODUCTION

Optical trapping is a useful technique in the field of single-molecule manipulation that is capable of applying forces on dielectric particles in the piconewton range and displacement measurements in the nanometer range. In molecular biology, one of the main uses of optical traps has been to study the mechanical and thermodynamic properties of nucleic acids such as DNA or RNA and proteins (1–3). In nucleic acid thermodynamics, the melting temperature (T_m) of DNA is defined as the temperature at which half of the DNA strands are in the double-stranded DNA (dsDNA) and single-stranded DNA (ssDNA) forms. For other applications, such as PCR and sequencing, it is important to accurately determine the T_m of the DNA.

Traditionally, the thermodynamic properties of DNA have been determined using bulk techniques such as calorimetry (4) and UV absorbance (5,6). In both cases, the T_m has been determined by changing the temperature or pH of the entire sample. Over the past two decades, single-molecule force spectroscopy has been established as a powerful, accurate, and bulk-complementary method to characterize the thermodynamics of nucleic acids. A major advantage of single-molecule methods is that they make it possible to characterize thermally induced fluctuations during thermodynamic transformations in individual molecules and small systems in general (7). In spite of their low number of degrees of freedom, small systems coupled to thermal baths (such as a single DNA molecule embedded in an aqueous environment) are tractable in the standard framework of equilibrium statistical mechanics, where concepts such as equilibrium free energy, enthalpy, and entropy are fully applicable (8). Mechanical melting, or unzipping, is a process that consists of pulling apart the two strands of the dsDNA until the basepairs are disrupted and the molecule converts into ssDNA (9,10). In this case, and in contrast to other techniques, force, rather than temperature, is used to open the molecule. Although force unzipping provides a direct estimate of free-energy differences, extracting the value of T_m always requires one to determine the entropy and enthalpy contributions. In general, the fate of many reactions in molecular biology (i.e., their affinity) is determined by the mutual compensation between the entropy and enthalpy contributions. For molecular weak interactions, such contributions are typically large compared with the affinity value itself: small variations in the entropy and enthalpy terms can modify the sign of the free-energy difference, reversing the direction of such reactions. This important property confers plasticity and adaptability to many regulatory pathways in the cell. For this reason, it is valuable to implement a temperature control function in an optical tweezers instrument, enabling it to measure free-energy differences at different temperatures to extract the enthalpy and entropy contributions.

Previous studies have utilized various methods of temperature control (11–15). Williams et al. (15) first used a Peltier heater-cooler device connected to the microchamber by

Submitted October 14, 2014, and accepted for publication May 12, 2015.

*Correspondence: ritort@ffn.ub.es

Sara de Lorenzo's present address is Instituto Madrileño de Estudios Avanzados en Nanociencia (IMDEA Nanociencia), Cantoblanco, 28049 Madrid, Spain.

Editor: Keir Neuman.

0006-3495/15/06/2854/11 $2.00

http://dx.doi.org/10.1016/j.bpj.2015.05.017

copper plates and 1.0-NA water-immersion objectives. However, force and distance measurements are less accurate with this type of lens. Mao et al. (12) used water immersion objectives similar to ours (NA = 1.2) with hot-cold circulating water collars in the objectives. The microchamber comes to the same temperature as the objectives because of heat conduction through the water immersion fluid. However, the objective lenses expand or contract by several microns with big changes in temperature, causing the optical trap to shift position by the same amount. A significant time (~30 min) is required for the instrument to stabilize at each new temperature, making it impractical to test the same individual molecule across a wide temperature range. Resistive heaters placed at the front of the objective lenses were used some time later to reduce the drift generated by fluid circulation (11,13).

As previously discussed (12,16–18), the advantages of using a local heating laser include the minimization of drift effects in the instrument. The wavelength of the heating laser was carefully chosen to generate heat in the bulk solution by infrared (IR) absorption without transmitting unnecessary extra heat to the objective lenses, effectively eliminating drift. Previous studies used the absorption of IR light in water as a method to heat rapidly and locally the surrounding medium (18–20). The use of IR absorption allows for full control of the heated volume as well as temperature changes over short periods of time. The heating laser we chose for our study operates at 1435 nm. It is readily absorbed, so it has a penetration depth of 315 μm in water (21,22). However, for a wavelength of 980 nm, as used in previous studies, the absorption depth is ~19,920 μm. Therefore, little of the incident light is absorbed in a water cell only 180 μm thick.

MATERIALS AND METHODS

Instrument design

The instrument used in this study is a miniaturized optical tweezers that uses counterpropagating beams with light-momentum force sensors capable of measuring force directly (23). All experiments were performed according to the scheme of Fig. 1 *a*, following previous work (10,12,23–26). In this approach, counterpropagating laser beams (Lumics LU845, λ= 845 nm and 150 mW at maximum power) are brought to the same focus through opposite microscope objective lenses (UPLASAPO 60XW, water immersion, NA 1.2; Olympus), generating a single optical trap. The molecular construct is then attached to a polystyrene bead held optically in the trap, which in turn acts as the force sensor, and to a second similar bead affixed by suction on the top of a micropipette. The molecular construct includes the DNA hairpin under study spliced between two dsDNA handles, which act as spacers to prevent nonspecific interactions between the bead and the DNA hairpin (Fig. 1 *b*). A third laser is introduced coaxially with the trapping lasers to generate heat (Alcatel A1948FBG, λ= 1435 nm and 160 mW at maximum power). The heating laser is a single-mode, fiber-coupled diode laser that is driven by a constant-current power supply. It is worth mentioning that our setup can also operate in the double-trap configuration, which is achieved by steering the trapping beams into two separated foci (27–29), thus avoiding the need to use a micropipette.

To work at low temperatures, we utilize a 1.5 m^3 top-opening refrigerator to freeze 20 L of water into a block of ice. The refrigeration is then turned off and the ice melts slowly, thus maintaining the temperature at a constant 4–5°C. The instrument head (10 kg) is lowered into the top of this icebox with a pulley mechanism and is suspended from an extension spring (stiffness 250 N/m) to isolate it from building vibrations. The instrument head does not touch the floor or walls of the icebox. It then takes the head ~3 h to equalize with the temperature inside the icebox. The head temperature (here designated as ambient) is measured using a thermal sensor installed close to the fluidics chamber. The light from the heating laser (located outside the icebox) to the instrument head is transmitted through 2 m of single-mode optical fiber (Fig. 1 *a*).

We could increase the temperature by 50°C above ambient by using full laser power (160 mW), and we also focused the heating laser into a small area of ~10 μm in diameter. However, such a small heated area creates a baseline shift in the light momentum force sensor due to refractive index changes in the heated water at the heating laser focus. That is, the 1435-nm heating beam can deflect the 845-nm trapping beams by heating water locally and changing its refractive index. Such refractive interference also occurs when the trap is empty (not occupied with a bead), indicating that the effect is not a tug-of-war between the heating and trapping beams. Rather, the pseudo-force between beams is repulsive due to the reduced refractive index of hot water.

To reduce such a baseline shift, we spread the heating beam out at the focus and changed its shape. Instead of focusing the heater to a point at the experimental plane, we use the heating equivalent of Köhler illumination (Supporting Material). Thus, the heating laser is focused to a point located at the back focal plane (BFP) of the objective lens so that the beam emerges into the experimental area collimated as a cylinder ~66 μm in diameter (Fig. S5). By changing to Köhler heating, the typical baseline shift is reduced from ~3 pN to only ~0.5 pN at full heating power.

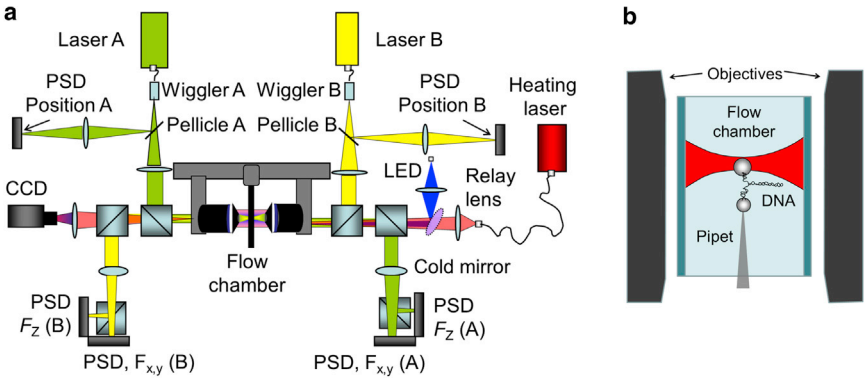

FIGURE 1 Schematic of the setup. (*a*) Counterpropagating optical trap with a light-momentum force sensor modified to include a temperature controller. The heating beam passes through a 45° dichroic long-pass filter (Edmund Optics 69-878), which acts as a cold mirror, thus reflecting the blue LED light, which illuminates the experiment, until a CCD camera and allowing the heating wavelength to pass through. (*b*) Single-molecule experiment. The DNA hairpin under study is attached between two polystyrene beads: one captured in the optical trap and the other held by air suction on the tip of a micropipette (see text for details). To see this figure in color, go online.

However, the maximum temperature increase at the experimental region is reduced to ~25°C above ambient temperature (Supporting Material). To extend the temperature range and to carry out experiments between 5°C and 30°C (cold measurements), the instrument is placed inside the icebox. For experiments conducted between 25°C and 50°C (hot measurements), the instrument is placed outside of the icebox by operating at room temperature.

The heating laser power is controllable between 0 and 160 mW with wavelength $\lambda = 1435$ nm and absorption coefficient, $\alpha(\lambda)$, between 31.0 and 31.7 cm^{-1} in water (22). This wavelength is very convenient for our experiments for two reasons: first, $\lambda = 1435$ nm does not interfere with the trap-lasers signal of 845 nm in the photodetectors because such silicon detectors have a spectral response between 500 and 1100 nm; second, the absorption coefficient for $\lambda = 1435$ nm in water is between 31.0 and 31.7 cm^{-1} (22). According to Beer's law, the loss in intensity due to adsorption as light travels through the medium is given by $I(x) = I_0 \exp(-\alpha x)$, where $\alpha(\lambda)$ is the adsorption coefficient and x is the distance the radiation travels through the medium. Thus, we can deposit a significant fraction (27%) of the incident beam power into our water layer, which is ~100 μm thick.

As noted by Mao et al. (12), one problem with local laser heating is that it generates convective fluid flow, especially in a chamber with a large vertical rise, such as a slide/coverslip oriented edgewise to gravity (so the laser beams can be horizontal). Then the hot water rises in the center and the cold water sinks at the edges in a continuous circuit flow up to 8 μm/s. This flow creates drag forces on tethered beads and also sweeps dirt from around the chamber into the trap, where it accumulates. To reduce such convection, we designed a new microfluidics chamber with reduced water thickness (110 μm instead of 180 μm) and a vertical cul-de-sac domed region that surrounds the pipette (Fig. 2 *a*). To measure the temperature around the trap, we followed the method described by Peterman et al. (18). By using the Stokes drag test on the trapped bead as a function of the heating laser power, and by knowing how the viscosity of the solution changes with temperature, we could extract the temperature of the surrounding medium (Supporting Material). We performed experiments on a DNA hairpin (Fig. 2 *b*) by using the new design of the chamber along with Cargille Labs refractive index matching liquid, series AAA, $n = 1.330$ (30), as immersion fluid between the chamber and objective lenses. This liquid is used on the objectives instead of water because 1) it evaporates much more slowly than water; 2) evaporation does not cool the chamber, so the external ambient temperature probe accurately represents the temperature at the chamber interior when the heating laser is turned off; 3) it absorbs no IR radiation at the heating-laser wavelength (30); and 4) it has lower thermal conductivity than water. Regarding the latter, the thermal conductivity (κ) is inversely related to the increase in temperature produced by a heating source. In particular, the increase in temperature upon heating (ΔT) depends linearly on the power delivered by the heating laser (P) being inversely proportional to the thermal conductivity of the medium (12,18), $\Delta T \approx P/\kappa$. The thermal conductivity of the Cargille fluid is 0.1 W/K (30) to be comparable to the thermal conductivity of water (0.6 W/K) and glass (1.1 W/K). The low thermal conductivity of the Cargille fluid contributes to minimize heat flow between the fluidics chamber and the objectives, keeping them isolated from potentially harmful heating effects.

Unfortunately, Cargille fluid has one-quarter the surface tension of water but 1.9 times the density, and thus is difficult to suspend between the objective lens and the coverglass due to gravity forces. To solve this problem, we used thicker #2 coverglasses for the new fluidics chamber. As a result, the distance between the coverglasses and the objective lenses was reduced and the Cargille fluid stabilized over longer times.

Instrument calibration

Smith et al. (23) described several methods to calibrate the light-momentum force sensor, including a light-flux photometric method and a thermal noise force test. However, the simplest calibration is done by using Stoke's law. Here, we translate the fluid chamber back and forth with a velocity v past a trapped sphere with radius r and measure the drag force F with the momentum sensor, which is then compared with Stokes' law, $F = 6\pi r\eta v$, where η is the viscosity of the surrounding water. Despite the simplicity of the formula, there are several issues that could affect the accuracy of the test, including 1) multiple peaks in the bead-size distribution, 2) the number of beads tested that are used to get a mean force, 3) deviations from sphericity in the bead distribution, 4) the proximity of chamber walls that affect the ideal behavior of the fluid, 5) viscosity changes due to the presence of salts in the buffers, 6) the temperature of the water, and 7) heating by the trapping lasers.

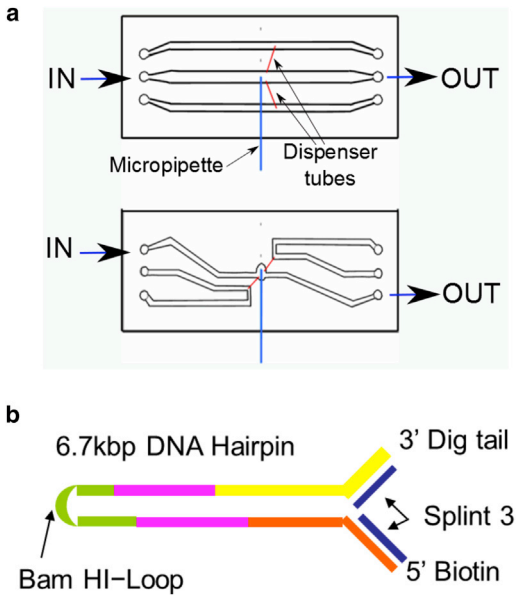

FIGURE 2 Chamber channels and DNA hairpin designs. (*a*) Scheme of the old (*upper panel*) and new (*lower panel*) microfluidics chamber designed to prevent convection. The new design employs two coverglasses (24 × 60 mm, #2; VWR 48382-139) and one Nescolfilm layer (instead of two as in the old design). With this design, the microchamber thickness is reduced from 180 to 110 μm. The channel design was modified to avoid obstruction of the lower channel by the micropipette (~80 μm in diameter). The central channel holds the micropipette in the dome (this cavity typically is 2 mm high and 1.8 mm wide). The direction of the flow, which is stopped during an experiment, is marked by IN and OUT labels. The top and bottom channels, connected to the main channel through dispenser tubes, are used to flow different types of beads and to control the concentration and flow speed at their entrance to the dome of the central channel. (*b*) Design of the 6.8 kb sequence. Details are provided in the Supporting Material. To see this figure in color, go online.

In brief, to circumvent the bead-related issues, we carried out drag experiments in a chamber with pure water using polystyrene microspheres that are specific for calibration, with a precise diameter of 3.00 ± 0.07 μm (microbead NIST traceable particle size standard, 3.00 μm, Cat. #64060, Polyscience; DISC calibration). We also accounted for wall effects, which become important in our thin chambers. According to Happel and Brenner (31), the drag coefficient is increased by 3% for a 3 μm bead in the center of a 100 μm chamber (Eq. S9). Viscosity changes due to dissolved salts were mainly treated according to measurements in the literature (32,33).

We determined the temperature spatial profile by using water viscosity changes (Fig. 3, *left*) and analyzing the thermal fluctuations of the optically trapped bead (Fig. 3, *right*; Supporting Material), and checked the data against a simple 1D heat-flow model (Eq. S8). In this model, the temperature exhibits a parabolic dependence within the heating laser spot and a

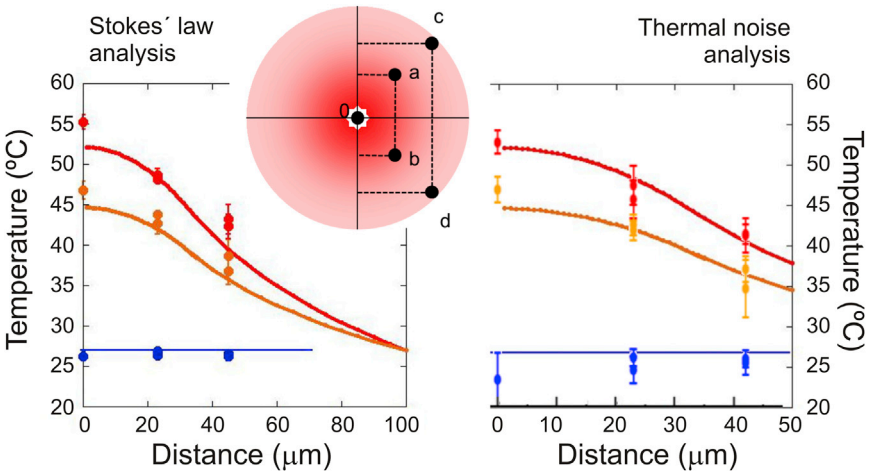

FIGURE 3 Temperature spatial profile of the heating laser beam. Measurements were taken at five different positions within the heating beam spot (see *inset*). (*a–d*) The distances from (*a*) and (*b*), and from (*c*) and (*d*) to the center of the screen are ~23 μm and ~42 μm, respectively. Red dots show the measured temperature at 5.7 mW inside the fluidics chamber (full heating laser power), and orange dots show the measured temperature at 4 mW. Blue dots show the measured temperature with the heating laser off. This measured temperature (~27°C) is taken as ambient for the 1D heat-flow model (Supporting Material), whose predictions are the red and orange continuous curves for 5.7 and 4 mW, respectively. Left graph: Stokes' law analysis; right graph: thermal noise analysis. To see this figure in color, go online.

logarithmic decay outside the spot (the latter trend was previously studied by Mao et al. (12)). Measurements obtained by the two methods are very similar and compatible with this simple model. Experiments with the DNA hairpin were performed across distances of <8 μm near the heating spot center, where temperature is homogeneous within 1°C.

Another possible use for the laser-heating method would be to study single-molecule kinetics after a sudden temperature change. In this case, the temperature rise time after the heating beam is switched on becomes an important parameter. We obtained an estimate for this time by using a finite-element 2D heat-flow simulation (Supporting Material) in which we mimicked the experimental geometry and materials (water, glass, and immersion fluid) with 10,000 discrete ring elements, each with a defined thermal conductivity and specific heat capacity. This simulation generates a steady-state radial profile similar to the 1D model (Fig. S6) even though much of the heat is conducted away laterally through the glass chamber walls rather than radially through the water (Fig. S7 a). The simulation also shows that the temperature reaches 90% of its final equilibrium value within 30 ms after the beam is initiated (Fig. S7 b). Unfortunately, we never achieved such short rise times experimentally because our laser power supply has a low-pass filter to prevent thermal shock to the emitting diode (Fig. S8). Perhaps a fast optical shutter would reveal an inherent 30 ms rise time. Koirala et al. (17) measured a rise time of only 5 ms in their T-jump optical trap, but with a high temperature gradient near their heated bead. In contrast, we needed a larger region of homogeneous temperature in which to unzip our 6.8 kbp hairpin and stretch it into ssDNA with an end-to-end distance of 7 μm.

Heating by trapping near-IR radiation has been examined in previous works (see Mao et al. (12) and references therein). Here, we used viscosity changes to estimate in situ an upper temperature rise of 0.9–1°C at maximum power due to water absorption at 845 nm.

RESULTS AND DISCUSSION

DNA as a local thermometer

To demonstrate the capabilities of the temperature-jump instrument, we carried out experiments in which single DNA molecules were unzipped at different temperatures ranging from 3°C to 45°C. Our molecular construct consists of a 6.8 kbp hairpin flanked by two 29 bp handles on the 3′ and 5′ ends (Fig. 2 *b*; see Supporting Material for details of the molecular construct and for a description of the unzipping setup). In Fig. 4 *a*, we present force-distance curves (FDCs) obtained during the unzipping process in 1 M NaCl at various temperatures. The unzipping-rezipping cycles show that the curves almost overlap, indicating that the experiments at a 50-nm/s pulling rate were reversible (quasistatic).

The stability of dsDNA with respect to ssDNA, as specified by the free-energy difference $\Delta G(T)$, is strongly dependent on T (15). Increasing T reduces the stability of dsDNA and promotes the melting process. By measuring the mean unzipping/rezipping force for different molecules and across the above-mentioned temperature range, we observed that the mean force decreased linearly with the temperature (Fig. 4 *b*). This is explained by the entropic contribution to the free energy of formation of the double helix, which destabilizes the double helix upon an increase in temperature. For each molecule, the temperature was measured and analyzed as described in the Supporting Material. Moreover, the zero force baseline, in any case always lower than 0.5 pN, was corrected for each trace. Using a simulation program (Supporting Material) to reproduce the unzipping experiments, we predicted the change of the mean unzipping/rezipping force versus temperature (Fig. 4 *b*; Table S2). In this simulation, we used either the nearest-neighbor (NN) basepair free-energy values for ΔH and ΔS (unified oligonucleotide (UO) values) (4) or those reported from unzipping experiments (HU values) (10). The parameters for the extensible freely jointed chain (ext-FJC) model were taken from Bosco et al. (34).

The experimental measurements of the forces are in agreement with the theoretical predictions at room temperature, with a difference in the mean force of ~2% (Table S2). However, below room temperature the discrepancy between the experimental results and the theoretical values predicted by HU is ~4%. This is not the case with the UO prediction, which shows a difference of ~1%. In contrast, at high temperatures, the discrepancy between the experimental results

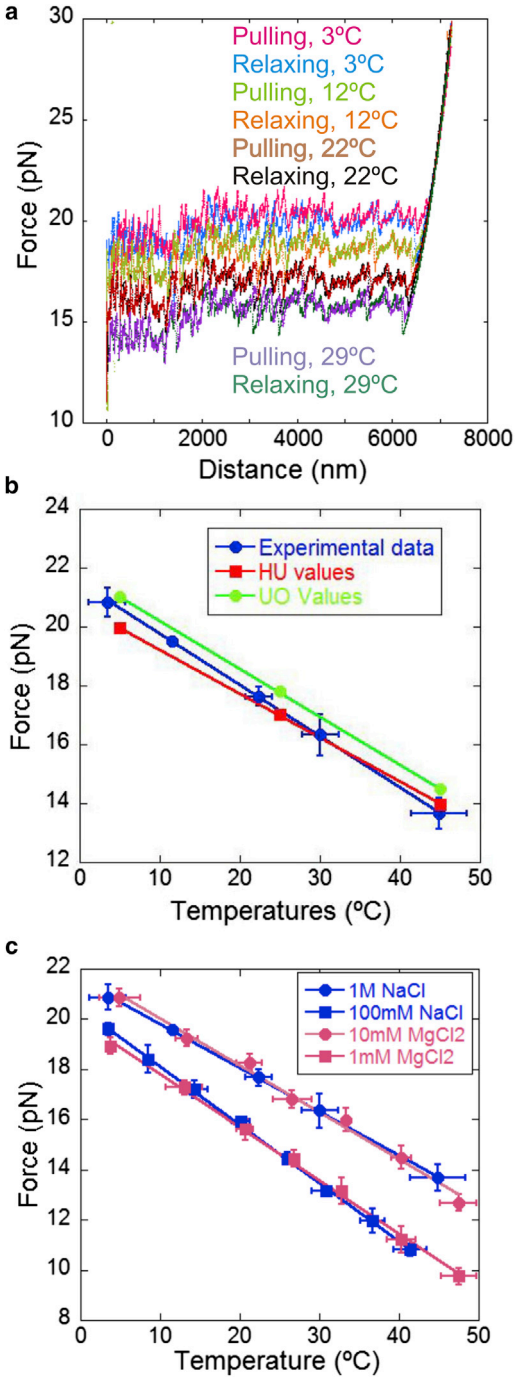

FIGURE 4 Unzipping experiments at different temperatures. (*a*) Force-extension curves (FECs) measured at 1 M NaCl + TE, pH 7.5. Here the cold measurements have been aligned to the hot segments, where the position-sensitive photodetectors operate at room temperature, by matching the unzipping measurements at 25°C. See Supporting Material. Unzipping and rezipping traces are almost identical, showing that the experiments were carried out under quasistatic conditions. (*b*) Mean unzipping/rezipping force versus temperature. Experimental data points, each averaged over four molecules at 1 M NaCl TE buffer, pH 7.5, are shown in combination with two theoretical predictions based on experimental data from (10) (HU) or SantaLucia (4) (UO; see also Table S2). (*c*) Mean unzipping/rezipping force versus temperature in different ionic conditions. Experimental data represent the average over eight molecules. These results remarkably follow the rule regarding a 1:100 ratio of monovalent to divalent salt, similarly to what has been observed for RNA (33). To see this figure in color, go online.

and the theoretical predictions is larger for the UO values, ~3%. Clearly, the slopes between the experimental data and the simulated data are different in Fig. 4 *b*.

Experiments were conducted in different buffer solutions (1 M NaCl, 100 mM NaCl, 10 mM $MgCl_2$, and 1 mM $MgCl_2$; Fig. 4 *c*). Unzipping forces are almost the same at 1 M NaCl and 10 mM $MgCl_2$ at 25°C. The same effect is observed for the solutions at 100 mM NaCl and 1 mM $MgCl_2$. This shows that the mean unzipping force follows the 1:100 rule regarding the ratio of monovalent to divalent salt, a trend that was also observed for RNA (35). The mean unzipping force is expected to vary proportionally with the logarithm of ionic strength; however, a 100-fold concentration of Na^+ is required to achieve the same unzipping force as compared with the Mg^{2+} case, indicating strong, nonideal effects in the binding affinity of counterions to DNA in solution.

Average basepair free energies from force melting experiments

Force melting experiments have been used in combination with Monte-Carlo techniques to derive the salt- and sequence-dependent basepair free energies in DNA (10). Here we discuss a simpler model to derive the average (sequence-independent) basepair free energies, enthalpies, and entropies at different temperatures.

We approximate the typical sawtooth pattern of the FDC in unzipping experiments by a horizontal line corresponding to the mean unzipping force, f_p (Fig. 5). In the plateau region, the extension of trap and molecular handles (x_T, x_h in Fig. 5) is approximately constant, so the change in the trap-to-pipette distance when moving from λ_1 to λ_2 corresponds to the increase in ssDNA length (Δx_{ss}), which is induced by the unfolding of n dsDNA basepairs, $\lambda_2 - \lambda_1 = \Delta x_{ss} = n\Delta x$ (where Δx is the length change induced by the unfolding of a single basepair). The configuration of the experimental setup along the FDC at two different distances is depicted in Fig. 5 (*top*, *green circles*). The area under the equilibrium FDC curve between the two distances is the reversible work, $W = f_p\,\Delta\lambda$, that is necessary to bring the system from distance λ_1 to distance λ_2 (W corresponds to the area of the *dashed rectangle* in Fig. 5). W equals the total free-energy change ΔG, which is the sum of a contribution due to the unfolding ΔG_0 (the average basepair free energy) and a contribution from the stretching of the ssDNA (this stretching free energy corresponds to the area below the *blue dotted line* in Fig. 5, with the line being the FDC of $2n$ bases of ssDNA). Equating the work and the free-energy change, we get

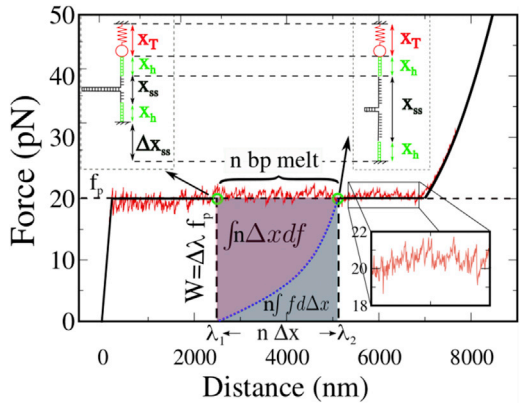

FIGURE 5 Calculation of mean basepair free energies from unzipping measurements. The configuration of the experimental setup at two different distances (λ_1, λ_2) is shown above the FDC. The sawtooth pattern (*inset*) is approximated by a straight line corresponding to the mean unzipping force (f_p). The force equals f_p at λ_1 and λ_2, so the extension of trap and molecular handles (x_T, x_h) stays constant. Different distances λ correspond then to different ssDNA extensions. The reversible work necessary to drive the system reversibly from λ_1 to λ_2 corresponds to the area in the dashed rectangle. Along this transition, n basepairs are disrupted, and the corresponding free-energy change involves both the basepairing free energy and the free energy due to stretching $2n$ bases of ssDNA. The basepair free energy can be recovered once the elastic contribution arising from stretching the ssDNA is subtracted from W (as detailed in the main text). To see this figure in color, go online.

$$W = f_p \Delta\lambda = \Delta G = n\Delta G_0 + \int f dx. \quad (1)$$

Integrating Eq. 1 by parts and using the fact that $\Delta\lambda = n\Delta x$ yields $n\Delta G_0 - n\int \Delta x df = 0$; hence,

$$\Delta G_0 = \int \Delta x df. \quad (2)$$

This integration by parts can be understood geometrically as the difference between the area of the dashed rectangle and the area under the dotted curve in Fig. 5. This is shown as a purple region in Fig. 5. According to Eq. 2, the average basepair free energy ΔG_0 can be computed from the definite integral of the force-extension curve of an unfolded basepair, taken up to the rezipping/unzipping plateau force. Therefore, to measure ΔG_0, it is necessary (besides measuring the mean unzipping force) to parametrize the temperature- and salt-dependent elasticity of ssDNA.

Analyzing the change in molecular extension with temperature

The elasticity of ssDNA can be measured from the unzipping pattern. We use the simulations (Supporting Material) that yield the number of basepairs corresponding to the different force peaks observed along the sawtooth pattern. From the experimental unzipping data, we can measure the distance between consecutive peaks at a given force and temperature, which is due to the difference in ssDNA extension. More in depth, the ratio between the measured distance and the number of basepairs between peaks provides the extension of ssDNA per basepair, Δx. This is a differential extension measurement, i.e., it is based on the measurement of differences in the trap position. As a consequence, it avoids the systematic error associated with the definition of the zero in absolute distance or molecular extension measurements. The zero for extension measurements is difficult to determine precisely in single-trap tweezers because a significant uncertainty results from the fact that the molecule can be attached anywhere on the surface of the immobilized bead in the pipette, a problem that needs to be solved to compare single molecules in different conditions (36–38).

Fig. 6 *a* shows unzipping traces for one molecule at two different temperatures (5°C and 29°C). After correcting for the experimental drift on the traces, we observe that the unzipping pattern shrinks as the temperature is raised (two *horizontal black arrows* in Fig. 6 *a*), implying that the ssDNA extension at the unzipping force changes with temperature. By repeating this measurement for different temperatures, we can determine the change in molecular extension between the helix and the coil state (Δx), and how this parameter varies with temperature. Fig. 6 *b* shows the extension per basepair versus temperature. Experimental unzipping results show that Δx decreases with increasing temperature. As in Fig. 4 *b*, the mean unzipping force also decreases with temperature.

Fig. 6 *c* shows the length change that occurs upon the unfolding of a basepair as a function of the mean unzipping force, which in turn is temperature dependent. Consequently, the change shown in Fig. 4 *a* is the combined effect of a change in force and temperature. To disentangle the effect of force from that of temperature in the previous measurements, we carried out a second set of measurements using a previously developed experimental methodology (34). In this approach, after the DNA hairpin has been completely unzipped, a 30-base oligo that selectively binds to the loop region of the DNA hairpin is flowed inside the fluidics chamber, blocking the rezipping. The oligo-bound molecule is then kinetically trapped in the ssDNA form. This method allows one to measure the ssDNA FDC down to low forces, where the duplex form would otherwise be preferred.

Fig. 7 a shows the FDC of one ssDNA molecule obtained by this method in the temperature range of 5–25°C. A shoulder is observed at low forces (<10 pN) due to nonspecific secondary structure formation. As previously described (10,23,34), this plateau is observed at low forces (<10 pN) and high salt (>100 mM NaCl). The effect of temperature on this plateau is clearly distinguishable (Fig. 7 *a*). The plateau height increases at decreasing temperatures. The compaction of ssDNA is apparent in the force shoulder that extends over the range of 5–10 pN. This shoulder

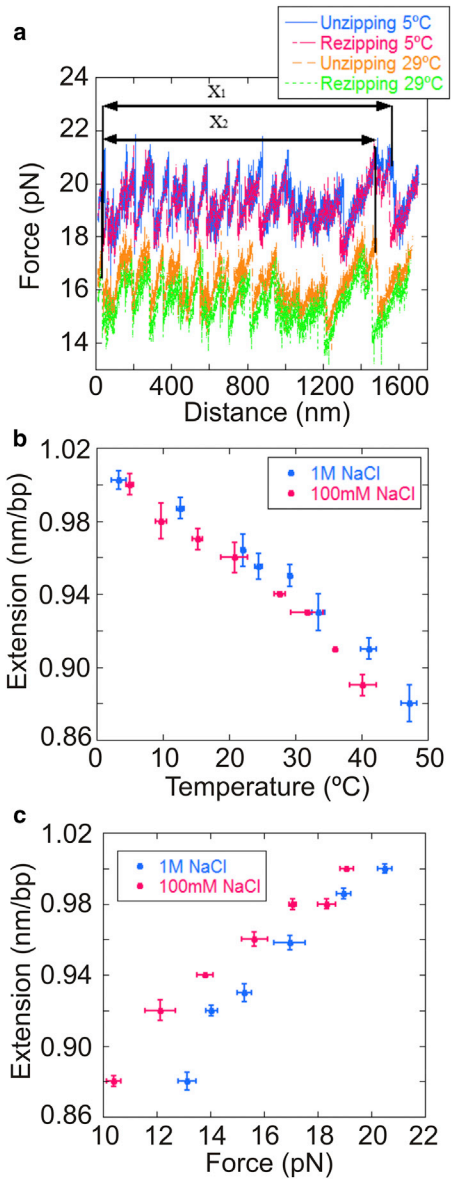

FIGURE 6 Dependence of the molecular extension of ssDNA on temperature and force. (*a*) Unzipping/rezipping traces for the same molecule at 5°C and 29°C. By measuring the change in distance between different peaks along an FDC (*horizontal black arrows*), we determine the molecular extension of the hairpin as a function of the temperature and force. (*b*) Extension/basepair versus temperature. Each dot represents the average over four molecules in either 1-M NaCl or 100-mM NaCl buffer solution. The force was not held constant; rather, the extensions were taken at the equilibrium zipping force, which varied with temperature, as shown in (*a*). Although the distance between basepairs does change with *T*, it does not appreciably change when the salt concentration is varied. (*c*) Extension/base versus unzipping force. Results were averaged over four molecules in either 1-M NaCl or 100-mM NaCl buffer solution. The distance between bases changes with force in both conditions. To see this figure in color, go online.

indicates the formation of secondary structures that are stabilized by lowering the temperature and increasing the salt. Similar effects on ssDNA were observed in previous works (39,40) and recently quantified for a wide range of monovalent and divalent ionic concentrations (34), but only Danilowicz et al. (41) showed that reducing the temperature produces the same condensation effect as a higher salt concentration.

To parametrize the elasticity of ssDNA at different temperatures, one must adopt an elastic model. Commonly used models to investigate the elastic properties of the ssDNA include the ext-FJC model (18), where the Kuhn length (L_K) is the parameter to determine, and the worm-like chain model (42,43), where the elasticity is governed by the persistence length (L_p).

Earlier studies (10,34,40) suggested that the ext-FJC is the best model to fit the parameters at different ionic concentrations, and hence we chose it for our analysis. The ext-FJC model considers the molecule as a chain formed by N rigid segments each of length L_K. The force-extension curve of the ext-FJC model follows the equation

$$x = L_c\left[\coth\left(\frac{fL_K}{k_BT}\right) - \left(\frac{k_BT}{fL_K}\right)\right]\left(1+\frac{f}{K}\right), \qquad (3)$$

where L_c is the contour length, L_K is the Kuhn length, and K is the stretching modulus. The value of L_c is determined by fixing the contour length of the molecule to 0.57 nm/bp (34). The total contour length is thus $L_c = 7857$ nm for a hairpin of 13,650 nt. Equation 3 was fitted to the experimental FDC at different temperatures. The fits were constrained with the data obtained from the peak-to-peak distance analysis and performed in the force range of 15–40 pN to avoid secondary structure formation. The results of the fits are shown in Fig. 7 *b*. The Kuhn length shows an approximately linear dependence on T (Fig. 7 *c*), whereas the stretch modulus is independent of temperature (Fig. 7 *d*). Remarkably, the change in Kuhn length is apparently compensated for by the change in temperature (Fig. 7 *c*, *inset*), so the ratio k_BT/L_K is constant in the explored temperature range.

Analyzing the *T* dependence of thermodynamic potentials for DNA melting

The parametrization of the temperature-dependent elastic properties of ssDNA discussed in the previous section can be used to compute the integral in Eq. 2 to derive the average basepair free energy. Experimental measurements enter Eq. 2 both through the mean unzipping force f_p and the elastic parameters, with the uncertainty in the former being the main contribution to the error on ΔG_0.

In Figs. 8 *a* and S14 *a*, the ΔG_0 obtained from Eq. 2 is compared with the average of the 16 heterogeneous NN basepair free energies given by the UO and HU predictions. Interestingly, our results interpolate between the UO and HU values, being fully compatible with HU at room temperature. Similar to what was observed for the mean

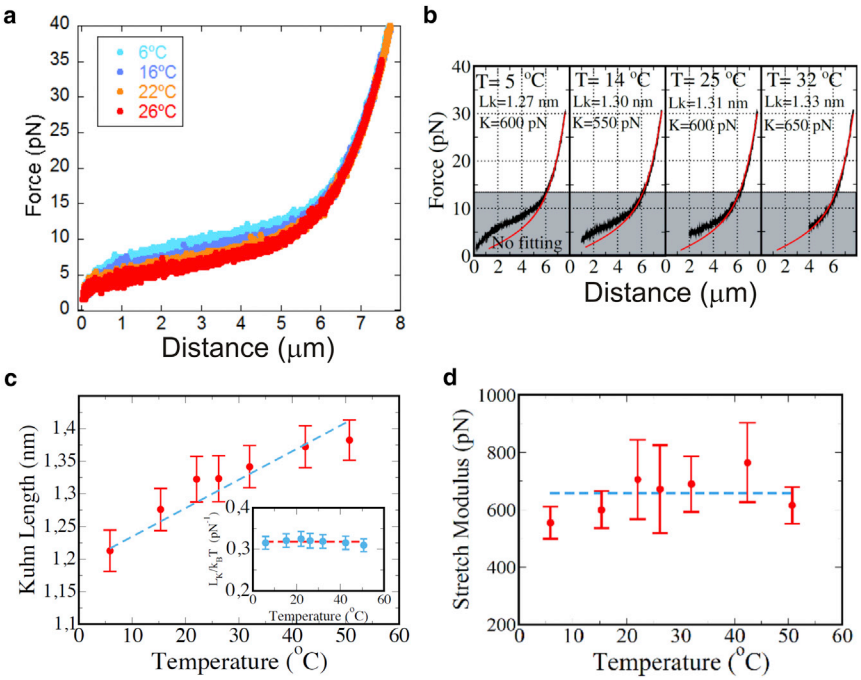

FIGURE 7 Temperature dependence of the single-stranded elastic response. (*a*) Cycles of pulling and relaxing curves of ssDNA at four different temperatures (6°C, 16°C, 22°C, and 26°C) and with 1 M NaCl, pH 7.5. The ssDNA was formed by using the oligo method (34). (*b*) The theoretical fit was obtained by using the ext-FJC model for forces in the range of 13–40 pN outside the dark gray region (labeled as *no fitting* in the legend). The experimental curves were taken at 1 M NaCl, pH 7.5. (*c*) Kuhn length (L_K) values for ssDNA at different temperatures and 1 M NaCl as a function of the temperature. Inset: Kuhn length scaled to the thermal energy level, k_BT. (*d*) Stretching modulus versus temperature for ssDNA measured at 1 M NaCl. In both panels, the dots represent the average at each temperature over six experiments, each with a different molecule. To see this figure in color, go online.

unzipping forces (see above), the measured free energies are in agreement with the UO values at low temperatures and with the HU values at high temperatures.

The thermodynamic stability of the DNA duplex is the result of a compensation of large entropy (ΔS) and enthalpy (ΔH) terms: $\Delta G = \Delta H - T\Delta S$. The new force-jump setup allows for experimental measurements of the entropy change (ΔS) and enthalpy change (ΔH) in the unfolding process. Along the transition line at constant force f_p, Eq. 2 reads $\Delta G_0(T) = \int_0^{f_p} \Delta x df$.

The entropy change, computed as the partial derivative of the free energy with respect to the temperature, gets a contribution from the basepair term, $\Delta S_0 = -\partial \Delta G_0/\partial T$ and from the force-dependent ssDNA stretching term, $\Delta S_{elas} = -\int \partial \Delta x/\partial T df$. Then

$$\Delta S = -\partial \Delta G/\partial T = \Delta S_0 - \Delta S_{elas}. \quad (4)$$

Calorimetric methods measure ΔS_0, and hence, for a direct comparison of our unzipping measurements with bulk measurements, the total entropy change should be corrected to account for the force-dependent elastic term ΔS_{elas}. However, as discussed in the previous section, the ratio k_BT/L_K is approximately constant (Fig. 7 *c*, *inset*) and the stretching contribution of ssDNA (as given by Eq. 3 and the integral appearing in ΔS_{elas}) varies slowly with temperature, so ΔS_{elas} can be neglected: $\Delta S \approx \Delta S_0$.

The entropy change ΔS can be derived directly from the Clausius-Clapeyron relation (40) (Supporting Material). For the mechanical melting transition, the Clausius-Clapeyron equation yields

$$\frac{\partial f_p}{\partial T} = -\frac{\Delta S}{\Delta x} \approx -\frac{\Delta S_0}{\Delta x}. \quad (5)$$

By neglecting ΔS_{elas}, we can measure the entropy change independently of the ssDNA elastic parameters. Equation 5 combines the slope of the force-versus-temperature curve shown in Fig. 4, *b* and *c*, with the Δx measurements shown in Fig. 6 *b*. The force-temperature curves of Fig. 4 *b* can then be used to compute entropy changes. Equation 5 implies that the difference in the measured entropy values is due to the different slopes of the lines shown in Fig. 4 *b*.

Using Eq. 5 to combine data from Figs. 4 *c* and 6 *b* yields data for Fig. 8, *b* and *c*. These figures show the enthalpy and entropy change as a function of the temperature, and Fig. S14 *b* shows the ratio between these thermodynamic potentials. The measured free energy, entropy, and enthalpy values at room temperature are shown in Table S3, and can be compared with those previously obtained for ssRNA (14). As far as the free energy is concerned, there is good agreement between our experimental values and those reported in the literature (4,10). On the contrary, SantaLucia's (4) measurements of entropy and enthalpy do not agree with our results, since our ΔS value is 5% higher than his. It must be noted that SantaLucia (4) derived the entropy from the free energy via T_m measurements (always relying on the two-state assumption and inaccurate determination of the melting point), whereas here we provide a more direct measurement of the entropy change. One problem with our method is that we measure local temperatures indirectly by changes in the hydrodynamic drag coefficient of a bead moving through water. Specifically, we equate the

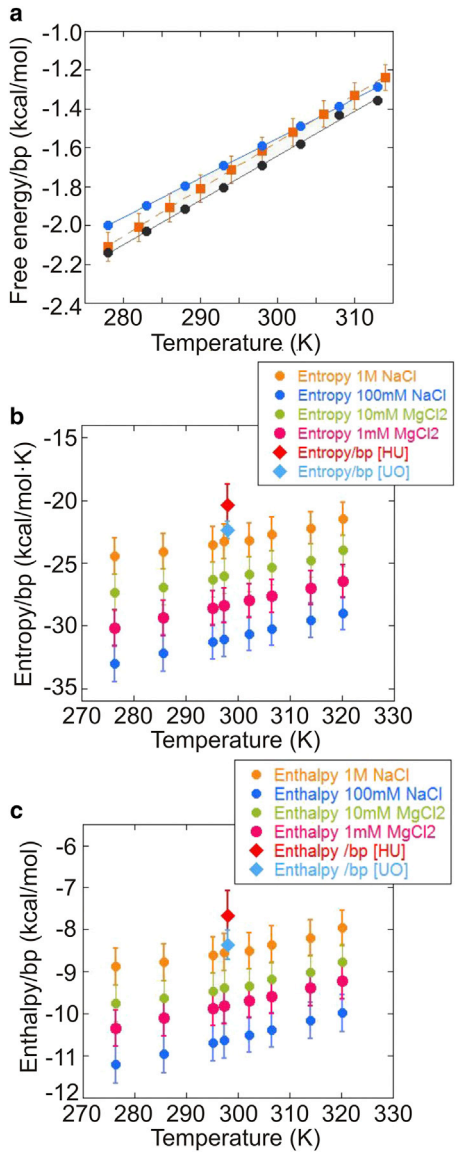

FIGURE 8 Average thermodynamic potentials versus temperature derived from DNA unzipping experiments. (*a*) Basepair free energy and comparison with UO (4) and HU (10) predictions at 1 M NaCl, pH 7.0. The orange squares show the experimental results calculated by fitting the elastic parameters as described in Supporting Material. The gray (*blue*) dots are average UO (HU) values for the free energy/basepair. (*b*) Basepair entropy as a function of temperature under different salt conditions. (*c*) Basepair enthalpy under different salt conditions. For comparison with the theoretical predictions, we also show the average of the entropies/enthalpies of the 16 NN motifs under standard conditions (1 M NaCl, 298 K) for the UO (*blue diamond*) and HU (*red diamond*) predictions. To see this figure in color, go online.

beam-center temperature for stationary water (when we unzip DNA) to the beam-center temperature when water is flowing past a test bead in a Stokes test. However, the introduction of cold water flowing past the Köhler heating beam should cause a small lateral shift in the heating profile and a reduction in temperature at the center of the beam. Therefore, we underestimate the temperature rise for the unzipping experiments, and consequently the slope of our plateau force-versus-temperature data (Fig. 4 *b*) appears too large. Suppose a flow velocity of 400 μm/s and an equilibration time of 0.03 s (Fig. S7 b) cause a shift of 12 μm in the temperature profile relative to the heating beam. Then, according to Eq. S8A, the temperature at the center beam would drop by 1° (4% of 25°C) and the experimental slope in Fig. 4 *b* would be 4% too high. Note that reducing the experimental slope by 4% makes it a rather good match to the UO-prediction slope (Table S2). In the future, it should be possible to check the temperature shift during flow more precisely by running a 3D simulation with ~1 million elements.

CONCLUSIONS

To our knowledge, we have developed a novel high-resolution temperature-jump optical tweezers instrument. The instrument covers a range of temperatures between 5°C and 50°C. Following the strategy put forward in previous studies (4,12,18,19), we used a heating laser to minimize the effects of instrumental drift. We carefully chose the laser wavelength to generate maximum heat in the bulk solution and transformed the focused beam geometry of the heating laser into a Köhler configuration to avoid convection effects and minimize force baseline shifts.

Using this strategy, we developed a temperature-jump optical tweezers with great thermal and mechanical stability. To test the viability of our temperature controller, we carried out a full thermodynamic characterization of DNA duplex formation by mechanically unzipping single DNA molecules at different temperatures. FDCs were measured under different temperature and salt conditions. The mean unzipping/rezipping force was found to decrease with temperature, as expected, due to the entropic contribution to the free energy of formation of the double helix, which is known to destabilize the double helix upon an increase in temperature.

We used the instrument to measure the average basepair free energy $\Delta G_0(T)$ in a range of temperatures between 5°C and 50°C. It was necessary to determine the temperature-dependent elastic properties of ssDNA because the work of stretching ssDNA appears to make a major contribution to the full reversible work measured along the unzipping FDC. Remarkably, we found that the persistence length of ssDNA appears to increase with temperature. This is at odds with the standard elastic rod model, which predicts that it should be inversely proportional to temperature. The persistence length of dsDNA was shown to decrease with temperature (44), but these two molecules have vastly different mechanics since one is stiffened by stacked basepairs and the other is stiffened mainly by electrostatic repulsion between phosphates. It is difficult to evaluate the full implications and generality of this result; however, it suggests that the elastic behavior of single-chain polymers (such as ssDNA, ssRNA, and polypeptide chains) is mostly

determined by electrostatic effects. Throughout this study we compared our experimental results with theoretical predictions given by the UO energies (4) and unzipping (HU) values (10). Our experimental results for the average basepair free energies agree with the theoretically predicted values (HU or UO) at room temperature. In contrast, the analysis of entropies and enthalpies highlighted significant differences with respect to those predictions. These discrepancies are attributed to systematic differences observed for the temperature-dependent free energy above and below room temperature. In fact, below room temperature there is a discrepancy of ~4% between the experimental results and the theoretical values predicted by HU. This was not the case with the prediction of UO values, which show a difference of ~1%. However, above room temperature the discrepancy between the experimental results and the theoretical predictions is larger for the UO values. These small but systematic discrepancies in free-energy measurements transduce into large discrepancies in the average entropy and enthalpy between our measurements and both UO and HU predictions.

The temperature-jump optical trap paves the way to obtaining a more detailed characterization of the thermodynamics of duplex formation in nucleic acids by deriving the 10 unique NN basepair free energies, enthalpies, and entropies at different temperatures from single-molecule unzipping experiments. Until now, this task could only be accomplished for basepair free energies via unzipping experiments at room temperature (10), and not for basepair-dependent enthalpies and entropies, which could be derived only indirectly from existing melting data on short (10–50 bp) oligos. The ability to control both force and temperature provided by the temperature-jump optical trap now makes it possible to directly measure basepair-dependent enthalpies and entropies at various temperatures. Our instrument may additionally shed light on two long-standing issues in the field of nucleic acid thermodynamics: measurement of the heat capacity change (and its temperature dependence) and characterization of the entropy-enthalpy compensation across the melting transition.

Promising future research directions include the characterization of the observed strong temperature dependence of secondary structure formation in ssDNA at low forces. Finally, although in this work we have only discussed experiments on DNA, our instrument can be used to manipulate any kind of biopolymer. As an example, we foresee the use of this instrument, in combination with fluctuation relations (27,43), to disentangle the entropic and enthalpic contributions in protein folding from pulling experiments under irreversible conditions. Given the importance of temperature in determining the fate of many chemical reactions and biophysical processes, we anticipate that temperature-jump methods, such as the one presented here, will be of great interest to the single-molecule community.

SUPPORTING MATERIAL

Supporting Materials and Methods, 14 figures, and three tables are available at http://www.biophysj.org/biophysj/supplemental/S0006-3495(15)00502-0.

AUTHOR CONTRIBUTIONS

S.L. and M.R.-C. performed research. S.L. and S.B.S. built the instrument. S.L., M.R.-C., and S.B.S. analyzed data. M.R.-C., J.R.A.-G., and S.B.S. contributed analytic tools. S.B.S. and F.R. designed research. S.L., M.R.-C., J.R.A-G., S.B.S., and F.R. wrote the article.

ACKNOWLEDGMENTS

The authors thank J. Camunas and S. Frutos for contributing the molecules used in the experiments, and J.M. Huguet for helpful discussion.

F.R. is supported by grant Institucio Catalana de Recerca i Estudis Avancats Academia 2013 and J.R.A.-G. by an Explora grant from MINECO (MAT2013-49455-EXP). The research that led to the results presented here was funded by the European Union Seventh Framework Programme (FP7/2007-2013) under grant 308850 INFERNOS and European Research Council grant MagReps (No. 267862).

SUPPORTING CITATIONS

References (45–48) appear in the Supporting Material.

REFERENCES

1. Arias-Gonzalez, J. R. 2013. Optical tweezers to study viruses. *Subcell. Biochem.* 68:273–304.
2. Arias-Gonzalez, J. R. 2014. Single-molecule portrait of DNA and RNA double helices. *Integr Biol (Camb).* 6:904–925.
3. Hormeño, S., and J. R. Arias-Gonzalez. 2006. Exploring mechano-chemical processes in the cell with optical tweezers. *Biol. Cell.* 98:679–695.
4. SantaLucia, Jr., J. 1998. A unified view of polymer, dumbbell, and oligonucleotide DNA nearest-neighbor thermodynamics. *Proc. Natl. Acad. Sci. USA.* 95:1460–1465.
5. Aboul-ela, F., D. Koh, …, F. H. Martin. 1985. Base-base mismatches. Thermodynamics of double helix formation for dCA3XA3G + dCT3YT3G (X, Y = A,C,G,T). *Nucleic Acids Res.* 13:4811–4824.
6. Plum, G. E., Y. W. Park, …, K. J. Breslauer. 1990. Thermodynamic characterization of the stability and the melting behavior of a DNA triplex: a spectroscopic and calorimetric study. *Proc. Natl. Acad. Sci. USA.* 87:9436–9440.
7. Bustamante, C., J. Liphardt, and F. Ritort. 2005. The nonequilibrium thermodynamics of small systems. *Phys. Today.* 58:43–48.
8. Nelson, P. 2004. Biological Physics. W.H. Freeman and Company, New York.
9. Bockelmann, U., P. Thomen, …, F. Heslot. 2002. Unzipping DNA with optical tweezers: high sequence sensitivity and force flips. *Biophys. J.* 82:1537–1553.
10. Huguet, J. M., C. V. Bizarro, …, F. Ritort. 2010. Single-molecule derivation of salt dependent base-pair free energies in DNA. *Proc. Natl. Acad. Sci. USA.* 107:15431–15436.
11. Luchette, P., N. Abiy, and H. Mao. 2007. Microanalysis of clouding process at the single droplet level. *Sens. Actuators B Chem.* 128:154–160.
12. Mao, H., J. R. Arias-Gonzalez, …, C. Bustamante. 2005. Temperature control methods in a laser tweezers system. *Biophys. J.* 89:1308–1316.

13. Mao, H., and P. Luchette. 2008. An integrated laser-tweezers instrument for microanalysis of individual protein aggregates. *Sens. Actuators B Chem.* 129:764–771.

14. Stephenson, W., S. Keller, …, P. T. Li. 2014. Combining temperature and force to study folding of an RNA hairpin. *Phys. Chem. Chem. Phys.* 16:906–917.

15. Williams, M. C., J. R. Wenner, …, V. A. Bloomfield. 2001. Entropy and heat capacity of DNA melting from temperature dependence of single molecule stretching. *Biophys. J.* 80:1932–1939.

16. Hormeño, S., P. Gregorio-Godoy, …, J. R. Arias-Gonzalez. 2014. Laser heating tunability by off-resonant irradiation of gold nanoparticles. *Small.* 10:376–384.

17. Koirala, D., J. A. Punnoose, …, H. Mao. 2014. Yoctoliter thermometry for single-molecule investigations: a generic bead-on-a-tip temperature-control module. *Angew. Chem. Int. Ed. Engl.* 53:3470–3474.

18. Peterman, E. J., F. Gittes, and C. F. Schmidt. 2003. Laser-induced heating in optical traps. *Biophys. J.* 84:1308–1316.

19. Braun, D., and A. Libchaber. 2002. Trapping of DNA by thermophoretic depletion and convection. *Phys. Rev. Lett.* 89:188103.

20. Holmstrom, E. D., and D. J. Nesbitt. 2010. Real-time infrared overtone laser control of temperature in picoliter H(2)O samples: "nanobathtubs" for single molecule microscopy. *J Phys Chem Lett.* 1:2264–2268.

21. Hale, G. M., and M. R. Querry. 1973. Optical constants of water in the 200-nm to 200-microm wavelength region. *Appl. Opt.* 12:555–563.

22. Palmer, K. F., and D. Williams. 1974. Optical properties of water in the near infrared. *J. Opt. Soc. Am.* 64:1107–1110.

23. Smith, S. B., Y. Cui, and C. Bustamante. 2003. Optical-trap force transducer that operates by direct measurement of light momentum. *Methods Enzymol.* 361:134–162.

24. Bosaeus, N., A. H. El-Sagheer, …, B. Nordén. 2012. Tension induces a base-paired overstretched DNA conformation. *Proc. Natl. Acad. Sci. USA.* 109:15179–15184.

25. Bustamante, C., and S. Smith. 2005. Light-force sensor and method for measuring axial optical-trap forces from changes in light momentum along an optic axis. U.S. patent 7, 133, 132, B2.

26. Smith, S. B., and C. Rivetti. 2010. TweezersLAB. http://tweezerslab.unipr.it.

27. Alemany, A., M. Ribezzi-Crivellari, and F. Ritort. 2013. Recent progress in fluctuation theorems and free energy recovery. *In* Nonequilibrium Statistical Physics of Small Systems. R. Klages, W. Just, and C. Jarzynski, editors. Wiley-VCH, Berlin, pp. 155–179.

28. Ribezzi-Crivellari, M., J. M. Huguet, and F. Ritort. 2013. Counter-propagating dual-trap optical tweezers based on linear momentum conservation. *Rev. Sci. Instrum.* 84:043104.

29. Ribezzi-Crivellari, M., and F. Ritort. 2012. Force spectroscopy with dual-trap optical tweezers: molecular stiffness measurements and coupled fluctuations analysis. *Biophys. J.* 103:1919–1928.

30. Cargille Laboratories, Inc.. 2003. Typical Characteristics. AST3421. Cargille Laboratories Inc., Cedar Grove, NJ.

31. Happel, J., and H. Brenner. 1983. Low Reynolds number hydrodynamics: with special applications to particulate media. Springer, Dordrecht, The Netherlands.

32. Ozbek, H. 2010. Viscosity of aqueous sodium chloride solutions from 0°C–150°C. Paper LBL-5931. Lawrence Berkeley National Laboratory, Berkeley, CA.

33. Swindells, J. F. 1982. Handbook of Chemistry and Physics, 62nd edition. National Bureau of Standards. CRC Press, Boca Raton, FL.

34. Bosco, A., J. Camunas-Soler, and F. Ritort. 2014. Elastic properties and secondary structure formation of single-stranded DNA at monovalent and divalent salt conditions. *Nucleic Acids Res.* 42:2064–2074.

35. Bizarro, C. V., A. Alemany, and F. Ritort. 2012. Non-specific binding of Na+ and Mg2+ to RNA determined by force spectroscopy methods. *Nucleic Acids Res.* 40:6922–6935.

36. Hormeño, S., B. Ibarra, …, J. R. Arias-Gonzalez. 2011. Mechanical properties of high-G.C content DNA with a-type base-stacking. *Biophys. J.* 100:1996–2005.

37. Hormeño, S., B. Ibarra, …, J. R. Arias-Gonzalez. 2012. Mechanical stability of low-humidity single DNA molecules. *Biopolymers.* 97:199–208.

38. Hormeño, S., F. Moreno-Herrero, …, J. R. Arias-Gonzalez. 2011. Condensation prevails over B-A transition in the structure of DNA at low humidity. *Biophys. J.* 100:2006–2015.

39. Dessinges, M. N., B. Maier, …, V. Croquette. 2002. Stretching single stranded DNA, a model polyelectrolyte. *Phys. Rev. Lett.* 89:248102.

40. Smith, S. B., Y. Cui, and C. Bustamante. 1996. Overstretching B-DNA: the elastic response of individual double-stranded and single-stranded DNA molecules. *Science.* 271:795–799.

41. Danilowicz, C., C. H. Lee, …, M. Prentiss. 2007. Effects of temperature on the mechanical properties of single stranded DNA. *Phys. Rev. E Stat. Nonlin. Soft Matter Phys.* 75:030902.

42. Bustamante, C., J. F. Marko, …, S. Smith. 1994. Entropic elasticity of lambda-phage DNA. *Science.* 265:1599–1600.

43. Ribezzi-Crivellari, M., and F. Ritort. 2014. Free-energy inference from partial work measurements in small systems. *Proc. Natl. Acad. Sci. USA.* 111:E3386–E3394.

44. Geggier, S., A. Kotlyar, and A. Vologodskii. 2011. Temperature dependence of DNA persistence length. *Nucleic Acids Res.* 39:1419–1426.

45. Forns, N., S. de Lorenzo, …, F. Ritort. 2011. Improving signal/noise resolution in single-molecule experiments using molecular constructs with short handles. *Biophys. J.* 100:1765–1774.

46. Svoboda, K., and S. M. Block. 1994. Biological applications of optical forces. *Annu. Rev. Biophys. Biomol. Struct.* 23:247–285.

47. Vogel, H. 1921. The law of the relation between the viscosity of liquids and the temperature. *Phys. Z.* 22:645–646.

48. Peyret, N. 2000. Prediction of nucleic acid hybridization: parameters and algorithms. PhD dissertation. Wayne State University, Detroit, MI.

Supporting Material:

A temperature-jump optical trap for single molecule manipulation

S. de Lorenzo,[†,‡,§] M. Ribezzi-Crivellari,[†] J. R. Arias-Gonzalez,[¶,‖] S. B. Smith,[††] and F. Ritort[†,‡,*]

[†]Departament de Física Fonamental, Universitat de Barcelona, Diagonal 645, Barcelona, Spain. [‡]Ciber-BBN de Bioingenería, Biomateriales y Nanomedicina, Instituto de Salud Carlos III, Madrid, Spain. [§]Current address, Instituto Madrileño de Estudios Avanzados en Nanociencia (IMDEA Nanociencia). Cantoblanco, 28049 Madrid, Spain. [¶]Instituto Madrileño de Estudios Avanzados en Nanociencia (IMDEA Nanociencia). Cantoblanco, 28049 Madrid, Spain. [‖]CNB-CSIC-IMDEA Nanociencia Associated Unit ‘‘Unidad de Nanobiotecnología’’, Spain. [††]Steven B Smith Engineering, Los Lunas, New Mexico, USA.

*Correspondence: ritort@ffn.ub.es

Supporting Material List

Document S1 (this document). It includes:

- Supplementary information:
    - Temperature measurement using viscosity change.
    - Estimation of the heating spot size.
    - Heating laser power measurements.
    - Heat flow model (1D, steady state)
    - Heat Flow Simulation (2D, kinetic)
    - Measuring the T-jump risetime
    - Instrument force calibration
    - Synthesis of the molecule
    - Description of the unzipping experiments
    - Simulation program for unzipping/rezipping curves
    - Experimental error on thermodynamic potentials.
- Fourteen figures.
- Three tables.

Temperature measurement using viscosity change

Stokes' law method. We measured the local temperature with a similar method to that used by Mao et al. (3) and by Peterman et al (4); namely, we used a trapped bead as a probe to detect changes in the viscosity of the water surrounding the bead. This method consists of two steps.

- We filled the fluid micro-chamber with an aqueous buffer and measured the ambient temperature of the chamber with a nearby sensor (Analog Devices AD590), which was previously calibrated against an RTD reference thermometer (Thermoworks THS-222-555). We then introduced a polystyrene bead into the calibrated optical trap. We used the motorized stage to move the chamber (and consequently the buffer fluid) in *x* and *y* axis with respect to the trapping beams and recorded the chamber velocity and force over the bead. Experimental data were plotted and linearly fitted, the slope, γ, of the regression yielding the drag coefficient at ambient temperature (Fig. S1 *a*). The viscosity at the particular ambient temperature, η_{room}, is extracted from tabulated data (1, 2), as plotted in Fig. S1 *b*.
- Using the same bead, we turned on the heating laser to a certain constant power and moved the motorized stage back and forth again while recording data of the chamber velocity and force over the bead. The slope, γ', of the linear fit is now lower because the viscosity of an aqueous solution drops with temperature (Fig. S1, *a* and *b*). The new fluid viscosity is $\eta_{room} \times (\gamma' / \gamma)$. The temperature is obtained by checking the new viscosity against tabulated data (1, 2).

This procedure removes uncertainties due to small deviations of the beads from sphericity or size errors. A Stokes' law force calibration of the instrument is carried out using pure water, however the DNA unzipping experiments are carried out in a buffer containing either NaCl (100 mM, 200 mM or 1 M) or $MgCl_2$ (10 mM or 1 mM). The ionic concentrations used in the experiments with $MgCl_2$ were so low that the viscosity of pure water was used in these cases.

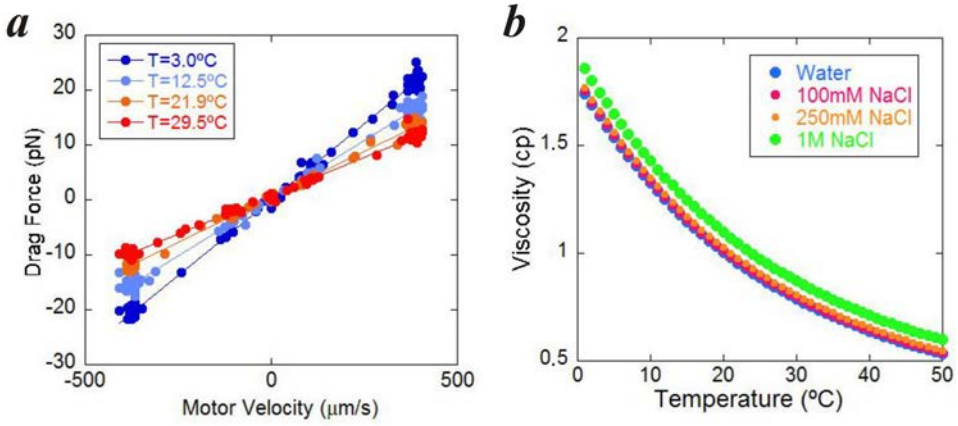

Fig. S1. Temperature measurements using viscosity changes. (*a*) Drag force vs. velocity at different powers. The corresponding temperatures, shown in the legend, were obtained as described above. The experiments were performed with a 3-μm diameter *calibration* bead in pure-water. As temperature increases the drag coefficient (proportional to the slope of the force-velocity curve) decreases. (*b*) Viscosity vs. temperature for distilled water at different [NaCl], according to two independent references, which data are similar (1, 2).

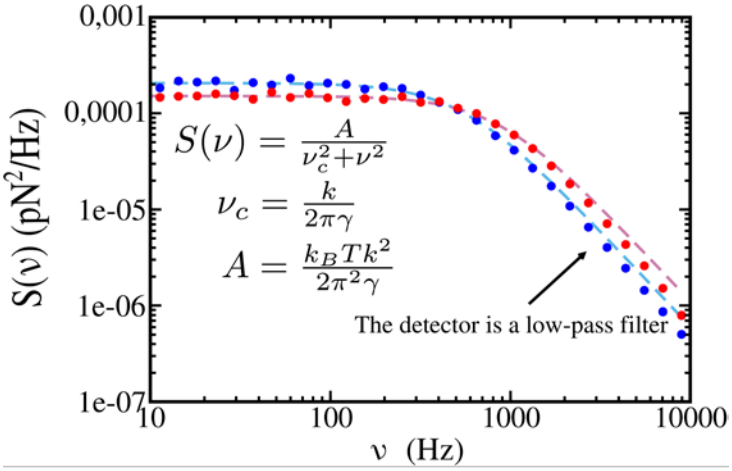

Fig. S2. Power spectrum density (PSD) of a 3-μm optically-trapped bead in distilled water. The experiments were carried out at maximum trapping (845-nm) laser power using calibration beads. Dots represent the experimental data and dashed lines are the Lorentzian fits (Eq. S1). Blue, heating laser off (fitted corner frequency, 541 Hz); red, heating laser at maximum power, 5.7 mW in the trapping region (fitted corner frequency, 859 Hz).

We also applied this method to measure the temperature rise generated by the optical trapping beams, which are weakly absorbed by water. We used both 845-nm lasers at high (80 mW) and low (20 mW) powers and observed that the difference in the drag coefficient were about 4%, which indicates a small temperature rise of 0.9-1 ºC.

Thermal noise method. The measurements of the thermal fluctuations of the trapped bead were performed at a 100-kHz acquisition rate using a Data Acquisition (DAQ) board (National Instruments PXI-1033). The analysis of the data has been carried out using the power spectrum density method (Fig. S2). This figure shows the power spectrum obtained by the Fourier transform of the thermal fluctuations, which has been fitted to a Lorentzian function,

$$\langle \Delta f^2(\nu) \rangle = S(\nu) = \frac{2\gamma k_B T \nu_c^2}{\nu^2 + \nu_c^2}, \tag{S1}$$

where ν is the frequency in Hertz, $\nu_c = \kappa/2\pi\gamma$ is the corner frequency, γ is the drag coefficient and κ is the stiffness of the trap. The stiffness of the trap when the heating laser is off is $\kappa = 0.087 \pm 0.004\, pN/nm$. If we assume that the stiffness does not depend on the temperature (see below), we can measure the viscosity from the corner frequency. The drag coefficient is obtained by imposing $\gamma = 6\pi\eta R_{eff}$, where R_{eff} is an effective radius which takes into account wall effects. Measurements with calibration beads yielded $R_{eff} = 1.77 \pm 0.04\, \mu m$. Then, temperatures can be recovered by using Vogel's formula (5):

$$T(\eta) = \frac{B}{\ln \eta - A} - C, \tag{S2}$$

where $A = -3.72$, $B = 579$ and $C = -137.5$, T is expressed in K and η in $mPa{\cdot}s$. From the temperature measurements in Fig. 3 *b* (main text), we can now check the hypothesis that the trap stiffness does not depend on the temperature. Using the relation $\kappa = \pi A/\nu_c k_B T$, where $A = k_B T k^2/2\pi^2\gamma$ and ν_c are extracted from the fitted data, we observe in Fig. S3 no systematic effect of the temperature or the position in the stiffness values.

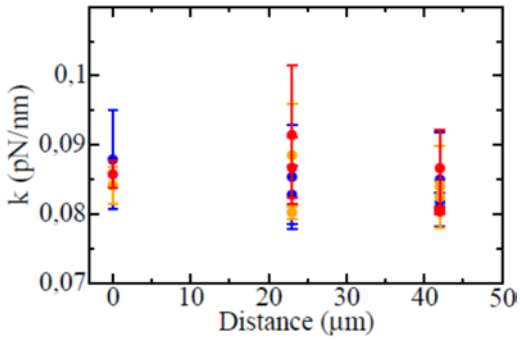

Fig. S3. Effect of temperature on trap stiffness. The graph shows measurements at different positions (see inset of Fig. 3 in the main text for details) and at different heating laser powers inside the fluidics chamber: red dots, 5.7 mW, yellow dots, 4 mW and blue dots, 0 mW (heating laser off).

Vogel's formula can be avoided if we measure the temperature from the force-fluctuations measurements. Specifically, we can use $T = \pi A/\nu_c k_B \kappa$ and the fitted parameters $A = k_B T k^2/2\pi^2\gamma$ and ν_c to obtain temperature data, assuming again that the stiffness does not depend on the force. With this thermometry method we do not require viscosity data but we have to measure the low-signal force fluctuations, which are prone to both calibration errors and distortions by low frequency noises.

The results of this analysis are shown in the graph below (Fig. S4). With the statistics obtained in these measurements, we cannot obtain a reliable temperature measurement. Nevertheless the measured temperature agrees qualitatively well with what was obtained using Vogel's formula and the thermal noise analysis. It is expected that with larger statistics the agreement improves.

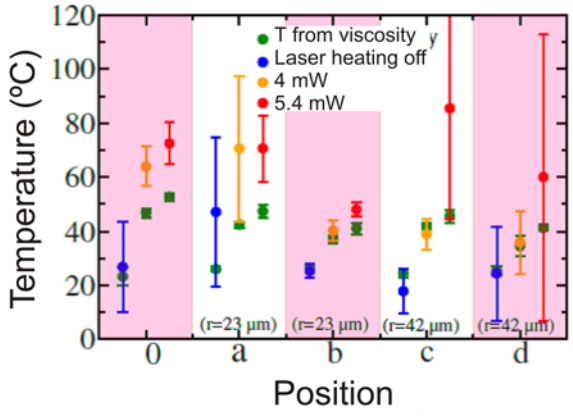

Fig. S4. Results of Temperature vs Distance from the center of the heating laser spot and comparison with the Vogel results. Heating laser powers are inside the fluidics chamber.

Estimation of the heating spot size

To determine the size of the Köhler illumination cylinder, we examine next the heating laser beam path before the microfluidic chamber (Fig. S5). As depicted, the heating laser light is coupled to the optical axis in our setup through an SM-28 optical fiber. Light exits the fiber in a cone with vertex angle θ such that the beam numerical aperture is $NA = sin(\theta/2) = 0.14$. The light cone expands over ~8.2 mm until it reaches an

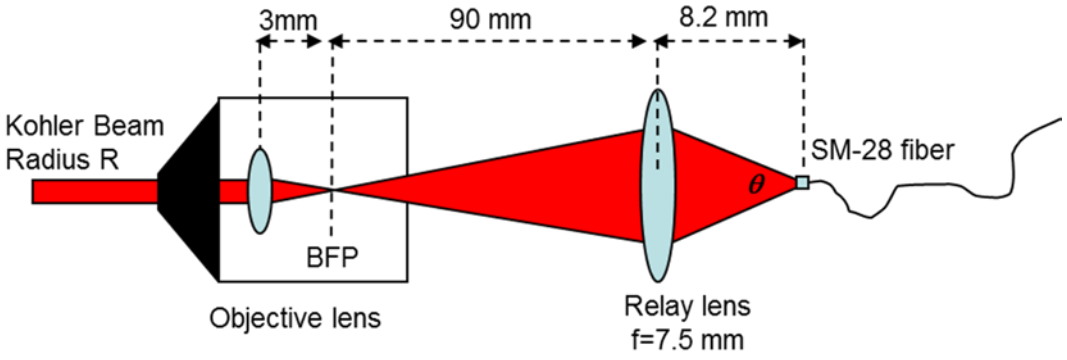

Fig. S5. Heating laser optical path. The beam expands from a single-mode optical fiber (SM-28) with a numerical aperture (NA) of 0.14 until a relay lens, where it is focused along 90 mm onto the back focal plane (BFP) of the first objective lens. Then, the narrow beam (NA=0.011) expands until it hits the 60X objective lens with effective focal length = 3 mm, where it is collimated into a cylinder with radius R=33μm, travelling across the microfluidics chamber until it reaches the front of the opposite objective lens (see the text for details). Three wavelengths (a blue LED illuminating the chamber, two counter-propagating 845-nm trapping lasers and a 1435-nm heating beam) share the optical path across the microfluidics chamber. Both the heating beam and the trapping laser that travels in the same direction are collected by the second objective lens and imaged onto a CCD camera. The wavelength of the heating laser is not visible with a silicon-target CCD; therefore a 905-nm auxiliary laser is incidentally used to estimate the size of the hot spot on the TV screen and to align it relative to the optical trap spot.

adjustable relay lens (Thorlabs CFC-8X). Then, the light is focused, entering the objective as a slightly convergent cone with initial radius of ~0.14×8.2 ≈ 1 mm. The relay lens distance can be tuned at ~90 mm for conjugate focusing to the back-focal plane (BFP) of the first objective. The numerical aperture of the convergent cone is thus $NA \approx 1/90 = 0.011$. Since the focal length of the objective lens is ~3 mm, the radius of the Köhler illumination cylinder is R ≈ 0.011 × 3 mm ≈ 33 μm.

Heating laser power measurements

We used a Thorlabs PM100 power meter with a Germanium slim photodiode power sensor (Thorlabs S132A) to determine how much heating power was delivered to the Köhler heating beam. Cargille immersion fluid (6) was used inside the chamber as well as between the microchamber and the objective lenses. An alignment check of the heating spot was conducted using a 905-nm laser, which can be monitored on a TV screen. The Germanium probe was installed between the prism box and the first objective lens. The process was repeated at the left objective lens exit.

At maximum laser current, the measured power after the second objective was 3.48 mW with Cargille fluid in the chamber. Therefore the input must have been 3.46 / 0.03125 = 111 mW. Although the maximum rated output for our heating laser is 160 mW, that power must then pass through 2 meters of optical fiber, a collimator lens, a dichroic mirror and two polarizing beamsplitter cubes before entering the first objective. Since each objective lens is identical, the maximum power in the center (Köhler heating beam) must have been $\sqrt{111 \times 3.48} = 19.7\,mW$. Note each objective lens transmits only 17.7% at 1435 nm.

TABLE S1 Heating-laser power measured at various points.

Switch positions	1	2	4	6	7	8	10	14	15
Drive current	91	167	295	400	445	482	555	670	695
Power in	11.7	25	47	65	72	(78.7)	(90.2)	(108)	(111)
Power out	0.36	0.76	1.48	2.02	2.25	2.46	2.82	3.38	3.48

First row indicates switch positions on laser power supply, which in the steady state yield a constant drive current (second row, in milliamperes) into heating laser. Third row shows power (milliwatts) entering first objective lens. Final row shows power (milliwatts) exiting 2nd objective lens after passing through chamber which was filled with Cargille fluid (absorbs nothing at 1435 nm). Due to sensor saturation it was not possible to measure more than 72 mW with the Thorlabs S132A probe. Therefore the larger input powers (shown in parentheses) were estimated from the corresponding output powers assuming a constant attenuation ratio (output/input) = 0.03125.

Now suppose we load water into the microchamber instead of Cargille fluid. Then the power in the beam will be partially absorbed and the transmitted power will follow Beer's law: $I(x) = I(0)\cdot\exp(-ax)$. Note that α, the absorption coefficient for water, is about 31.4 cm^{-1} (7) and the thickness of water in a typical chamber is 0.011 cm. Therefore the transmission will be 71% and the absorption 29%. Assuming maximum laser power where $I(0)$ = 19.7 mW , the absorbed power will be 5.7 mW.

Heat flow model (1D, steady state)

We assume that the heat flows radially, perpendicular to the laser beam axis and outward the Köhler-illumination geometry, as defined by a cylinder of radius R and length L. The *heat power* transferred across two coaxial cylindrical surfaces with radii r and $r + dr$ is:

$$P = -\kappa A \frac{dT}{dr}, \tag{S3}$$

where P is the light power absorbed by water, κ is the thermal conductivity of water, A is the surface area of the cylinder ($A = 2\pi rL$) and dT is the temperature change between the two cylindrical surfaces. The *heat flux density* (power per unit area) through the shell surface is equal to the total light power absorbed inside the shell divided by the surface area of the shell, $Q = P/A$. Eq. S3 then reads

$$dT = -\frac{Q}{\kappa} dr. \tag{S4}$$

The heat flux density is:

$$Q = \begin{cases} \dfrac{Pr}{2\pi R^2 L}, & r \le R, \quad \text{(S5A)} \\ \dfrac{P}{2\pi r L}, & r > R\,. \quad \text{(S5B)} \end{cases}$$

Integrating Eq. S5A for $0 < r < R$ and Eq. S5B for $< r < +\infty$, we obtain

$$T(r) = \begin{cases} T_0 - \dfrac{P}{4\pi L\kappa}\dfrac{r^2}{R^2}, & r \le R, \quad \text{(S6A)} \\ T(R) - \dfrac{P}{2\pi L\kappa}\ln\dfrac{r}{R}, & r > R\,, \quad \text{(S6B)} \end{cases}$$

where 'ln' is the natural logarithm. To apply the boundary conditions, on the one hand, we note that integrating dT outside the radius R to a distance r=+∞ yields an infinity temperature drop. The usual procedure in such problems is to cut off the integration at r=L, the length of the cylinder. Then, $T(L) = T_{room}$ in Eq. S4B implies that $T(R) = T_{room} + (P/2\pi L\kappa)\ln(L/R)$, being T_{room} the room temperature. On the other hand, we must impose the continuity at $r = R$, which implies that $T(R) = T_0 - (P/4\pi L\kappa)$. Therefore, the constant T_0 in Eq. S4 is given by:

$$T_0 - T_{room} = \frac{P}{2\pi L\kappa}\left(\ln\frac{L}{R} + \frac{1}{2}\right). \tag{S7}$$

By defining the temperature increment with respect to the ambient temperature, $\Delta T = T - T_{room}$, we express the solution of the problem as follows:

$$\Delta T(r) = \begin{cases} \dfrac{P}{2\pi L\kappa}\left[\ln\dfrac{L}{R} + \dfrac{1}{2}\left(1 - \dfrac{r^2}{R^2}\right)\right] & r \le R, \quad \text{(S8A)} \\ \dfrac{P}{2\pi L\kappa}\ln\dfrac{L}{r}, & r > R, \quad \text{(S8B)} \end{cases}$$

In our experimental configuration, P=5.7 mW at the maximum laser power (see section above), the distance between the chamber walls is L≈100 μm, the radius of the heating cylinder, R=33μm (previous section), the thermal conductivity of water $\kappa \approx$ 0.58 W/m·K and the ambient temperature, T_{room}=25 ºC. The blue line in Fig. S6 plots Eq. S8 under these conditions.

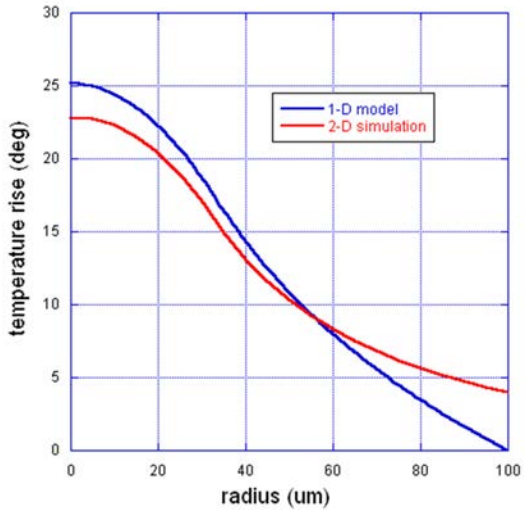

Fig. S6. Temperature profiles derived from different models. Blue line: 1D model where input power is 5.7 mW, L=100 μm and R=33 μm. Red line: 2D simulation where input beam power is 19.7 mW so 29% = 5.7 mW is extracted according to Beers law. R=30 μm and L=110 μm.

Heat Flow Simulation (2D, kinetic)

A heat-flow simulation was created that uses finite elements with specified material properties, e.g. for water, glass and Cargille fluid. In contrast to the 1D model above, each element in this 2D model is specified by a radius plus a lateral position parallel to the optic axis. Such ring-shaped elements can extend through the water, chamber walls, immersion fluid and up to the objective lenses. No arbitrary cutoff is required in the radial direction to limit the temperature rise at the center because lateral heat flow serves as a radial cutoff.

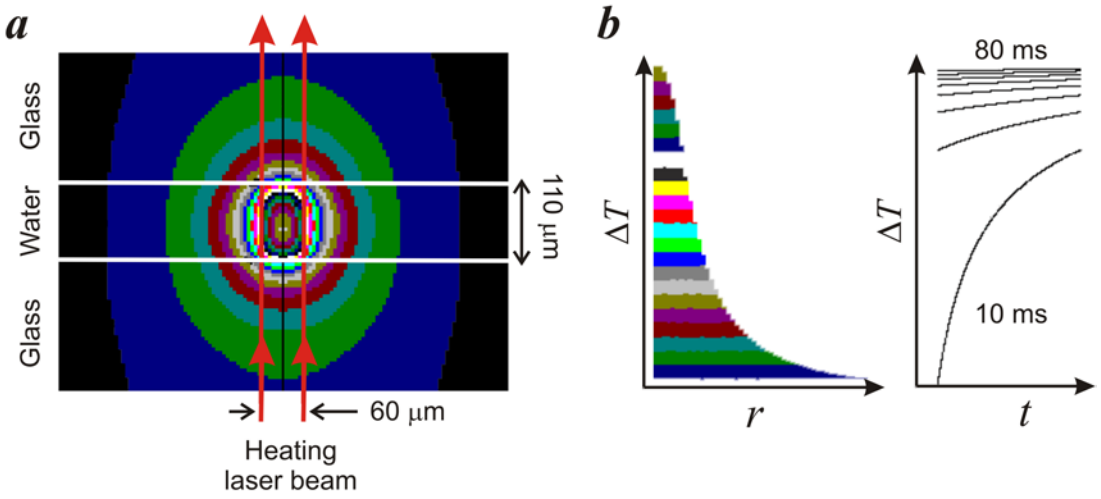

Fig. S7. Simulated heating pattern. (*a*) Temperature distribution due to radiation absorbed at the intersection of a 60 μm diameter heating laser beam and 110 μm water layer. Glass coverslips are drawn at top and bottom regions. Black color indicates a temperature rise less than 1 °C above ambient. Each new color represents an additional 1-degree rise. (*b*) Left, radial temperature profile in multiple colors. Such profile grows in height with time. Right, black curves follow the temperature at the center of the beam versus time. Each curve segment spans a time of 10 ms. Here, 8 successive curves represent 80 ms during which the center temperature has reached a steady state. In this example at time=30 ms the simulated temperature reached 90% of its final value, and at time=80 ms it reached 98%.

Our 2D simulation, Figs. S6 and S7, is "kinetic" because the finite elements have specific heat capacities and it takes time for heat to flow into an element by conduction and the temperature to rise. Heat is conducted both radially and laterally between adjacent rings. Time progresses in 4-μm steps, thus allowing characterization of transient responses when the heating beam is instantly turned on.

Source code and sample outputs can be downloaded at http://tweezerslab.unipr.it/cgi-bin/mt/software.pl/Search.

Measuring the Temperature-jump risetime

The temperature-jump rise time can be checked by using a DNA hairpin as a local thermometer. To do this we held the trap position constant while measuring the equilibrium rezip/unzip force while the temperature changed. Figure S8 shows the unzipping force of a DNA hairpin during a time when the heating power was altered by changing the heating-laser drive current. Under these conditions the risetime was about 200 ms which is 7 times longer than predicted by the simulation. Note the laser power supply had an RC filter to prevent sudden changes in the drive current. That filter comprises a 1 ohm metering resistor, 1 ohm dynamic laser-diode resistance, and a 0.056 farad capacitor. Then RC = 2×0.056 = 0.112 seconds. Therefore we were not able to observe the intrinsic delay for heating the water and glass chamber with an instant power pulse.

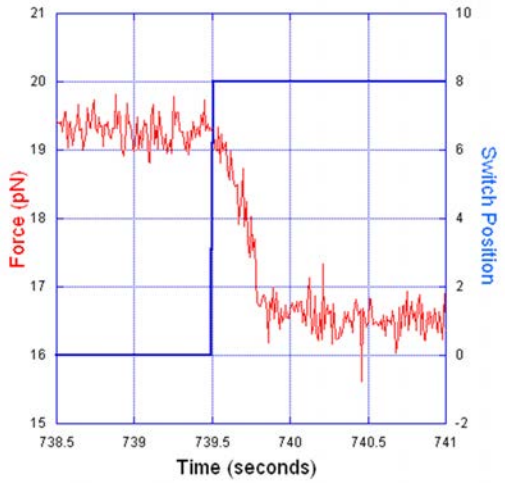

Fig. S8. Measurement of temperature rise-time. Red line is equilibrium zip/unzip force of DNA hairpin in 100 mM NaCl, at 5 ^{o}C above ambient. Blue line indicates switch position on heating laser power supply. Switch=zero delivers zero drive current into heating laser. Switch=8 initiates a drive current of 482 mA (see table S1).

Instrument force calibration

The calibration of force through viscosity changes was performed in a chamber with pure water using polystyrene microspheres that are specific for calibration, with a precise diameter (Polyscience ref Microbead Nist Traceable particle size standard 3.00 µm Cat# 64060 - DISC calibration). These microspheres have a nominal diameter of 3.00 ± 0.07µm. A single peak in the centrifuge insures a single peak in the size distribution. Our bead distribution has CV = 2.2%. Measuring a set of N beads will reduce the likely error (computed mean minus true mean) by a factor of $\sqrt{N}$. Reducing our likely error down to a 1% requires measuring five beads on average.

To make one such measurement, a single microsphere is captured in the optical trap. The micro-chamber is mounted on a stage platform in the optical tweezers instrument that can be moved along the *x*-*y*-*z* axis. By measuring the velocity at which the chamber is moved and by knowing the viscosity of water and the size of the bead, it is possible to calculate the force on the particle using Stokes' law (Fig. S9 *a*). This method is used to calibrate force along each axis (x, y, z). Usually the drag coefficients for a bead are in good agreement for all three directions. However if the trapped bead is oblate, or it has some dirt attached, then the *z*-axis drag appears lower because the extra bead mass aligns with the trapping-beam axis (*z*-axis) and this configuration presents lower fluid drag in the *z*-axis direction. Such beads can be excluded from the calibration.

Stokes' law measurements have been carried out using both the old and new microchamber designs (Fig 2*a*, main text). Interestingly, our experimental results, Fig. S9 *b*, demonstrate that if we use the Stokes' law as a method of force calibration, the proximity of the bead to the wall of the microchamber coverglass is an important aspect to consider. This effect, known as Faxen's law, could be defined as a correction to the shear viscosity and viscous drag coefficient of a microsphere in a viscous fluid sitting close to a wall (8). In our case, the bead in the trap is in close proximity to the two coverglass walls comprising the microchamber. For this reason we have corrected the expression for the viscous drag coefficient by using the Happel correction (9) for a microsphere of radius *r* and separation between walls of 2*h*:

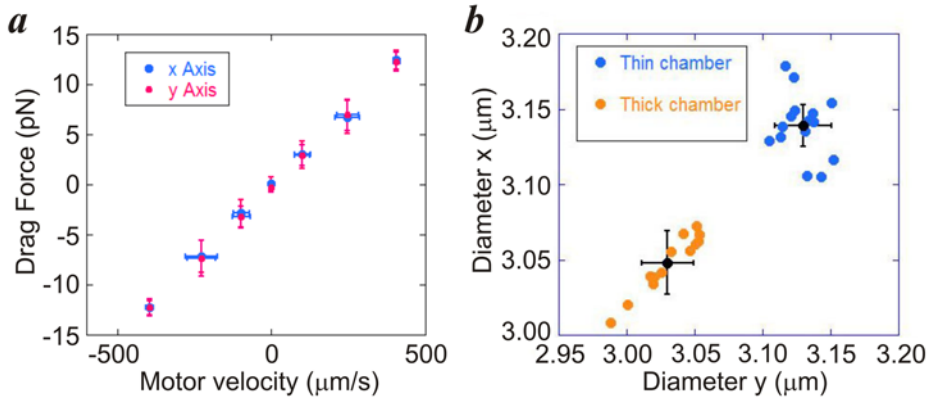

Fig. S9. Force calibration using Stokes' law. (*a*) Drag force vs motor velocity in x and y axes. Experiments were performed in pure water using special microspheres for calibration. The points showed in this graph correspond to a single bead and have been obtained by taking the average over the raw data. (*b*) Diameter measured along the x-axis vs diameter along y-axis by Stokes' law using the standard expression for the drag coefficient $\gamma = 6\pi\eta r$ where *r* is the bead radius. Data were obtained by measuring over 10/15 beads. The mean diameter measured in the thick chamber along the x-axis is 3.05 ± 0.019 μm and 3.03 ± 0.021 μm along the y-axis. The mean diameter measured in the thin chamber along the x-axis is 3.14 ± 0.021 μm and 3.13 ± 0.014 μm along the y-axis. Two different batches of calibration beads were tested with the same results. The difference observed between mean diameters evidences the importance of the Happel correction to the drag coefficient.

$$\gamma = \frac{6\pi\eta r}{1 - 1.004(r/h) + 0.418(r/h)^3 - 0.21(r/h)^4 - 0.169(r/h)^5} \qquad \text{(S9)}$$

Equation S9 predicts a change of a +3% for a 3-μm diameter bead in a 100-μm thick chamber. Therefore this correction was necessary for accurate calibration.

As formerly described (10, 11), the calibration of a momentum-flux force sensor depends on the sensitivity of its position-sensitive photodetector. In our instrument, both the fluid chamber and the silicon detectors cool to 4 ºC when the instrument head is lowered into the icebox. Therefore we did an experiment to check the force calibration at low temperatures by measuring the Stokes drag force on our calibration beads in cold conditions (4 ºC water, heating laser off). We found that the photodetector reading increased by a factor of 1.69 over the case where the photodetector and water were held at room temperature (25 ^{o}C). However literature values (2) show that water viscosity increases by a factor of 1.76 between those two temperatures. Therefore the momentum sensor under-reported the test force by ~4% of reading at low temperature, consistent with such a reduction in photodetector sensitivity. Thus the force calibration must be corrected by +4% for *cold experiments* compared to *hot experiments*, regardless of the state of the heating laser, which does not affect the detectors.

Synthesis of the molecule

The molecular construct consists of a long, 6838-bp DNA stem from λ-DNA (12) (New England Biolabs) with a tetraloop at the end of the hairpin (Fig. S10). To extract the DNA segment, a digestion of the λ-DNA phage with the BamHI restriction enzyme was carried out. The target of BamHI (New England Biolabs) is 5'-GGATCCC-3' and therefore this enzyme cleaves λ-DNA at several specific places. We are interested in the

segment between 41,732−48,502 bases, which forms the stem of the DNA hairpin (the cosR end). The DNA stem, the two 29-bp handles (13) and the tetraloop (3'-ATCA-5') are ligated to the cosR end and the previously modified Bam HI end. The role of the tetraloop is to prevent the separation of the two strands when the DNA hairpin is unzipped. To join the tetraloop, a self-complementary oligonucleotide, which forms a tetraloop on one side and a cohesive Bam HI end at the other, is ligated to the BamHI end of the DNA construction. To generate the DNA handles, an oligonucleotide (previously modified with several digoxigenins by using DIG Oligonucleotide Tailing Kit, 2nd Generation, Roche) is hybridized with a second 5' biotin-modified oligonucleotide. This DNA construction is complementary to cosR end and two identical 29-nucleotide long ssDNA at the other end. The two ssDNA are hybridized with a third oligonucleotide which is complementary to them resulting in two dsDNA handles. These handles are attached to the DNA construction by ligation reaction. The sample is kept in a 10-mM Tris-HCl, 5-mM EDTA buffer.

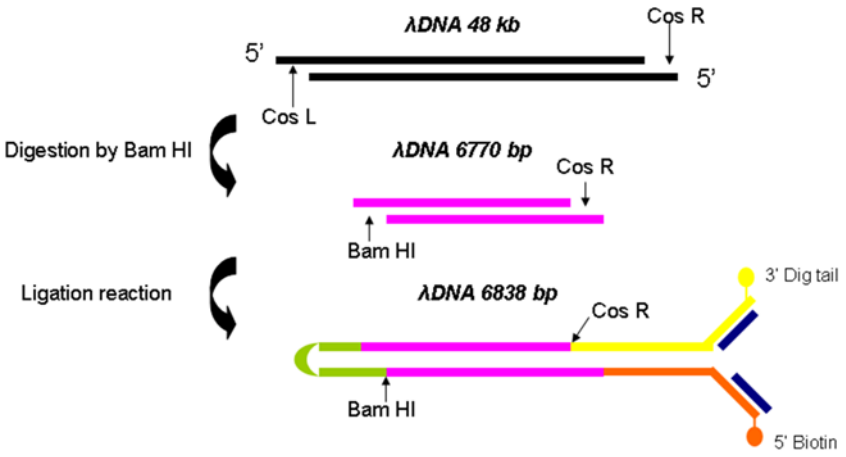

Fig. S10: Scheme of the synthesis of the DNA hairpin with closing tetraloop and dsDNA handles for the optical tweezers experiments.

The two handles are functionalized with biotin on one side and digoxigenin on the other. To unzip DNA, the DNA construction is attached to two polystyrene beads. One bead is coated with Streptavidin (SA) (G.Kisher GbR, ∅=2.0-2.9μm). The SA bead binds to the biotin-labeled handle of the molecular construction. The other microsphere is coated with protein G (Spherotech, Libertyville; ∅=3.0-3.2 μm), which is in turn cross-linked covalently with the anti-digoxigenin (AD) (Roche Applied Science) polyclonal antibodies through DMP. The AD bead binds to the digoxigenin labeled handles. To ease the binding between the hairpins and the AD beads, they are incubated together for 15 min in a TE buffer solution.

Description of the unzipping experiments

The unzipping experiments were carried out using the above explained DNA molecular construction in TE buffer (Tris 10 mM, pH 7.5) supplemented with either NaCl (1 M and 100 mM) and 1-mM EDTA or $MgCl_2$ (10 mM and 1 mM) as follows:

An SA bead is fixed on the tip of the micropipette by air suction and an AD bead is optically trapped (Fig. S11). The optical trap is moved relative to the bead fixed in the micropipette and the distance between them decreases until the beads rub together.

Then, by moving the beads apart, it is possible to check if the connection between the hairpin and the two beads has been created. DNA unzipping is generated by increasing the force applied to the strands of the molecule. When the applied forces reach a critical value, basepairs are disrupted hence creating the characteristic sawtooth pattern (see Fig. 4 *a* in the main text). This pattern is composed of peaks of different shapes and sizes (12). Pulling rates were about 50 nm/s . When the molecule was fully unzipped, the elastic response of the ssDNA was observed at the end of the curve.

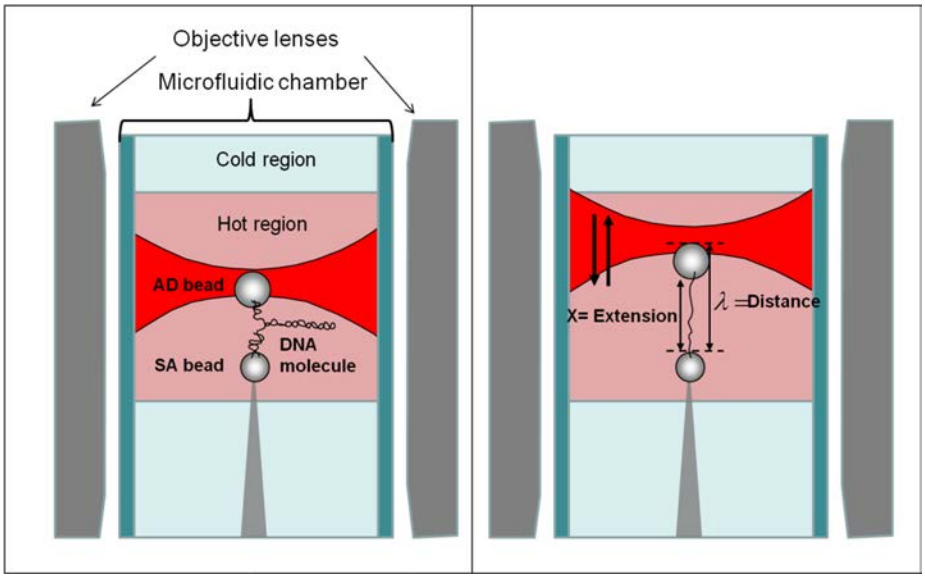

Fig. S11. Schematic representation of the unzipping experiments (not to scale). The light red ("hot region") corresponds to the volume heated by the heating laser. The light blue ("cold region") is the volume at ambient temperature.

Simulation program for unzipping/rezipping curves

Program Tweez13E is a Brownian dynamics simulation for the mechanical zipping of a DNA hairpin molecule attached to a bead in an optical-trap. The output is a Force-Distance Curve (FDC) characteristic of the chosen base sequence and input temperature. Different pull/relax cycles exhibit slightly different FDCs due to randomly generated thermal forces (Fig. S12). Pull / relax cycles also display force hysteresis that increases with pulling speed. Below is a simplified code example from the main loop:

```
repeat
   time:=time+dt ;      {dt = 1e-6 sec}
   getMoleculeTension;  {bead position, chain length, WLC model}
   zipHairpin(tension); {move fork position up or down 1 basepair}
   sumForcesOnBead;     {molecule tension + Brownian + optical}
   moveBeadInTrap;      {Langevin Eqn for overdamped particle}
   trackLightForce;     {assumes linear trap, stiffness = kSpring}
   moveTraps;           {to scan through length of molecule}
until scan=finished
```

The simulation programs can be downloaded from http://tweezerslab.unipr.it/cgi-bin/mt/software.pl/Search. They were written and compiled with Borland Turbo Pascal 7 and they will run on most 32-bit PC computers with an XP operating system.

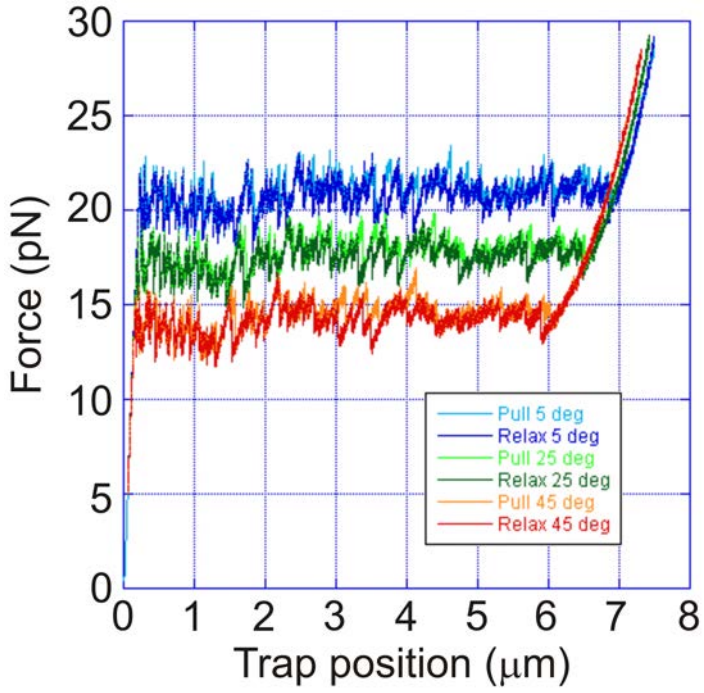

Fig. S12. Simulation output from TWEEZ13E for a 6.8-kbp hairpin assuming Santa Lucia et al. 1998 energy values in 1 M NaCl. Note that the ssDNA curves at the right end are longest for low temperature (blue) and shortest for high temperature (red). This is an example of rubber elasticity using the extensible-FJC model with a constant Kuhn-segment length. Therefore the experimental behavior (Figs. 4 *a* and 7 *a* in the main text) is surprising because there all the ssDNA extensions coincide above 25 pN, regardless of temperature.

Experimental error on thermodynamic potentials.

The homogeneous base-pair free energy was determined from the integral of the ssDNA FDC in the main text:

$$\Delta G_0 = \int (\Delta x/\mathrm{bp})\, df = L_c \int \left[\coth\left(\frac{f L_K}{k_B T}\right) - \frac{k_B T}{f L_K}\right]\left(1 + \frac{f}{K}\right) df \qquad \text{(S10)}$$

The four measured parameters are the mean unzipping force, f, the Kuhn length, L_K, the contour length, L_0, and the stretch modulus, K. Their errors affect the uncertainty in our free energy measurements. In Fig. S13 *a*, we show the different contributions to the free energy error as a function of f assuming a 5% relative error in the different parameters. These contributions to the error are computed by propagation:

$$d\Delta G_0 = \frac{\partial \Delta G_0}{\partial \alpha_i} d\alpha_i, \qquad \text{(S11)}$$

with $\alpha_i = f, L_K, L_0, K$. The uncertainty in force measurement is clearly the dominant term, the other ones having a low influence in the total error. A similar approach can be used to estimate the relevance of the force-dependent elastic contribution to the entropy change:

$$\Delta S_{elas} = \int \frac{\delta(\Delta x/\mathrm{bp})}{\delta T} df\,. \qquad \text{(S12)}$$

This entropy contribution can be rewritten as:

$$\Delta S_{elas} = -\frac{\partial \Delta G_0}{\partial L_K}\frac{\partial (L_K/k_B T)}{\partial T} - \frac{\partial \Delta G_0}{\partial K}\frac{\partial K}{\partial T}. \quad \text{(S13)}$$

From Fig. S13 *b* we conclude that $L_k/k_B T$ and K do not vary more than 10% over the temperature range we explored so we can estimate $\partial K/\partial T < 2\ pN/K$ and $\frac{\partial (L_K/k_B T)}{\partial T} = 0.0003\ (pN\ K)^{-1}$. With these estimations, we provide upper bounds to the elastic contributions to the entropy and validate the fact that we neglected these contributions in the main text.

In Fig. S13 *b* we show the two different contributions to ΔS_{elas} (one for $L_k/k_B T$ and one for K). Clearly the elastic contribution to the entropy change is below the experimental error on the total entropy change measured via the Clausius-Clapeyron equation and can be neglected in our measurements of ΔS_0.

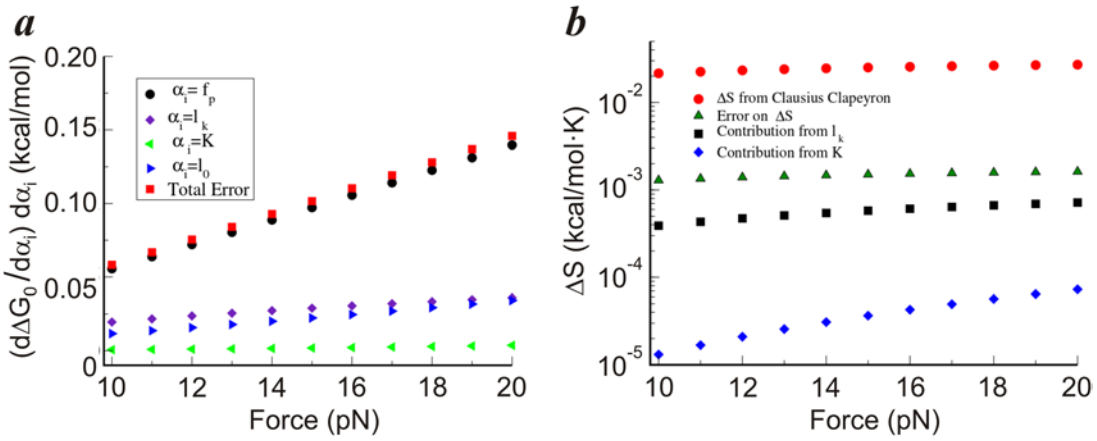

Fig. S13. Error contributions to thermodynamic potentials as a function of force. (*a*) Free energy change. (*b*) Entropy change.

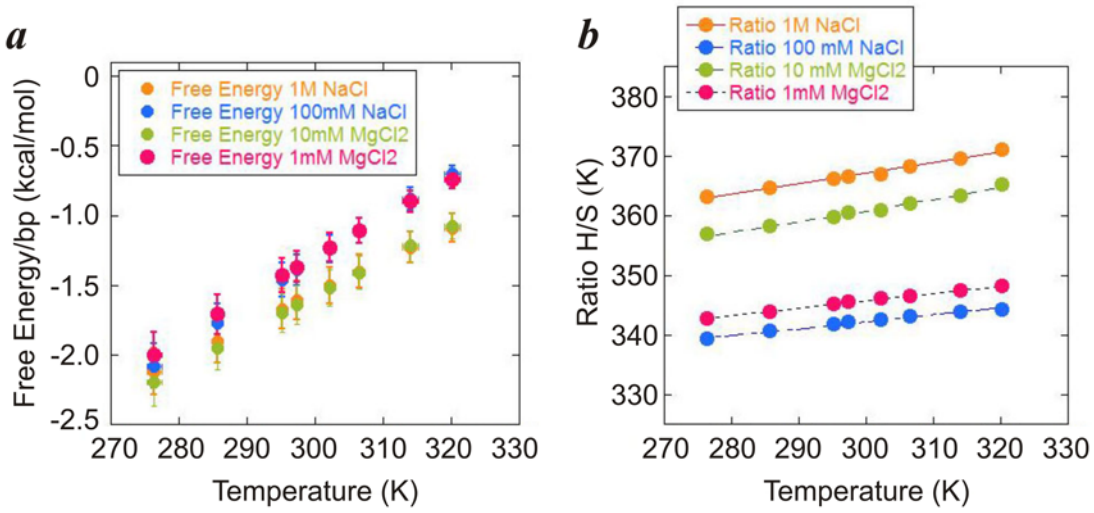

Fig. S14. (*a*) Base-pair free energies at different salt conditions. (*b*) Ratio between enthalpies and entropies at different salt conditions.

TABLE S2 Relation between the mean Mean Force and the temperature.

	Mean Force		
T (ºC)	**Exp results**	**HU Prediction**	**UO Prediction**
5	20.6 ± 0.5	19.9 pN	20.9 pN
15	18.9 ± 0.1	18.4 pN	19.2 pN
25	17.2 ± 0.3	16.9 pN	17.6 pN
35	15.4 ± 0.4	15.4 pN	16.0 pN
45	13.7 ± 0.5	13.9 pN	14.3 pN

Experimental data combined with two theoretical predictions. Exp results (Experimental results), HU Prediction (Based on unzipping measurements, Huguet et al. 2010), UO Prediction (Unified Oligonucleotide based on bulk melting measurements, Santa Lucia et al. 1998). The mean values of the experimental results were obtained averaging over 8 molecules at 1 M NaCl condition of salt.

TABLE S3 Thermodynamic potentials at room temperature (298K).

	F (pN)	Δx/bp (nm)	ΔG/bp (kcal/mol)	ΔS/bp (kcal/(mol K))	ΔH/bp kcal/mol
			1 M NaCl		
Exp values	17.1 (0.8)	0.95 (0.06)	-1.61 (0.15)	-23 (1.)	-8.5 (0.4)
HU values	16.9 (0.8)	0.95 (0.06)	-1.6 (0.14)	-20 (1.)	-7 (0.4)
UO values	17.6 (0.9)	0.95 (0.06)	-1.7	-22.1	-8.3
			100 mM NaCl		
Exp values	14.6 (0.7)	0.94 (0.04)	-1.38 (0.11)	-31. (1.3)	-10.6 (0.4)
HU values	14.8 (0.7)	0.94 (0.04)	-1.3 (0.14)	-20. (1.)	-8 (1)
UO values		0.94 (0.04)	-1.4	-23	-8.3
			10 mM $MgCl_2$		
Exp values	17.1 (0.8)	0.95 (0.06)	-1.6(0.14)	-26.(1.4)	-9.3 (0.4)
HU values	16.7 (0.8)	0.95 (0.06)	-	-	-
UO values		0.95 (0.06)	-1.7	-22.0	-8.3
			1 mM $MgCl_2$		
Exp values	14.6 (0.7)	0.94 (0.04)	-1.36 (0.11)	-28.4 (1.4)	-9.8 (0.4)
HU values	15.1 (0.7)	0.94 (0.04)	-	-	-
UO values		0.94 (0.04)	-1.4	-22.1	-8

Comparison between experimental (Exp Values) and theoretical (UO and HU, where available) values for the thermodynamic potentials at room temperature in four salt conditions (1 M NaCl, 100 mM NaCl, 10 mM $MgCl_2$ and 1 mM $MgCl_2$). HU refers to the prediction by Huguet et al. (2010), UO refers to the prediction by the MFOLD server, based on (14, 15). The temperature dependence of the measured thermodynamic potentials is shown in Fig. 8.

Supporting References

1. Ozbek, H. 2010. Viscosity of aqueous sodium chloride solutions from 0ºC-150ºC. Lawrence Berkeley National Laboratory. Paper LBL-5931.
2. Swindells, J. F. 1982. Handbook of Chemistry and Physics CRC 62edition. National Bureau of Standards.
3. Mao, H., J. R. Arias-Gonzalez, S. B. Smith, I. Tinoco, Jr., and C. Bustamante. 2005. Temperature control methods in a laser tweezers system. Biophys J 89:1308-1316.
4. Peterman, E. J., F. Gittes, and C. F. Schmidt. 2003. Laser-induced heating in optical traps. Biophys J 84:1308-1316.
5. Vogel, H. 1921. The law of the relation between the viscosity of liquids and the temperature. Phys. Z. 22:645-646.
6. Series AAA n=1.33 ref "AST3421, June 2, 2003. Typical Characteristics". Cargille Laboratories Inc., 55 Commerce Rd. Cedar Grove, NJ. 07009 USA.
7. Palmer, K. F., and D. Williams. 1974. Optical properties of water in the near infrared. J. Opt. Soc. Am. 64:1107-1110.
8. Svoboda, K., and S. M. Block. 1994. Biological applications of optical forces. Annu Rev Biophys Biomol Struct 23:247-285.
9. Happel, J., and H. Brenner. 1983. Low Reynolds Number Hydrodynamics: With Special Applications to Particulate Media. Springer Netherlands.
10. Bustamante, C., and S. Smith. 2005. Light-force sensor and method for measuring axial optical-trap forces from changes in light momentum along an optic axis. U.S.A. patent 7, 133, 132, B2.
11. Smith, S. B., Y. Cui, and C. Bustamante. 2003. Optical-trap force transducer that operates by direct measurement of light momentum. Methods Enzymol 361:134-162.
12. Huguet, J. M., C. V. Bizarro, N. Forns, S. B. Smith, C. Bustamante, and F. Ritort. 2010. Single-molecule derivation of salt dependent base-pair free energies in DNA. Proc Natl Acad Sci U S A 107:15431-15436.
13. Forns, N., S. de Lorenzo, M. Manosas, K. Hayashi, J. M. Huguet, and F. Ritort. 2011. Improving signal/noise resolution in single-molecule experiments using molecular constructs with short handles. Biophys J 100:1765-1774.
14. SantaLucia, J., Jr. 1998. A unified view of polymer, dumbbell, and oligonucleotide DNA nearest-neighbor thermodynamics. Proc Natl Acad Sci U S A 95:1460-1465.
15. Peyret, N. 2000. Prediction of Nucleic Acid Hybridization: Parameters and Algorithms PhD dissertation. In Department of Chemistry. Wayne State University, Detroit, MI.